

The impact of chemistry on the structure of high- z galaxies

A. Pallottini^{1,2,3,4*}, A. Ferrara^{4,5}, S. Bovino⁶, L. Vallini⁷, S. Gallerani⁴,
R. Maiolino^{2,3}, S. Salvadori^{8,9,10}.

¹ *Centro Fermi, Museo Storico della Fisica e Centro Studi e Ricerche “Enrico Fermi”, Piazza del Viminale 1, Roma, 00184, Italy*

² *Cavendish Laboratory, University of Cambridge, 19 J. J. Thomson Ave., Cambridge CB3 0HE, UK*

³ *Kavli Institute for Cosmology, University of Cambridge, Madingley Road, Cambridge CB3 0HA, UK*

⁴ *Scuola Normale Superiore, Piazza dei Cavalieri 7, I-56126 Pisa, Italy*

⁵ *Kavli IPMU, The University of Tokyo, 5-1-5 Kashiwanoha, Kashiwa 277-8583, Japan*

⁶ *Hamburger Sternwarte, Universität Hamburg, Gojenbergsweg 112, D-21029 Hamburg, Germany*

⁷ *Nordita, KTH Royal Institute of Technology and Stockholm University, Roslagstullsbacken 23, SE-10691 Stockholm, Sweden*

⁸ *Dipartimento di Fisica e Astronomia, Università di Firenze, Via G. Sansone 1, Sesto Fiorentino, Italy*

⁹ *INAF/Osservatorio Astrofisico di Arcetri, Largo E. Fermi 5, Firenze, Italy*

¹⁰ *GEPI, Observatoire de Paris, PSL Research University, CNRS, Place Jule Janssen 92190, Meudon, France*

ABSTRACT

To improve our understanding of high- z galaxies we study the impact of H₂ chemistry on their evolution, morphology and observed properties. We compare two zoom-in high-resolution (30 pc) simulations of prototypical $M_{\star} \sim 10^{10} M_{\odot}$ galaxies at $z = 6$. The first, “Dahlia”, adopts an equilibrium model for H₂ formation, while the second, “Althæa”, features an improved non-equilibrium chemistry network. The star formation rate (SFR) of the two galaxies is similar (within 50%), and increases with time reaching values close to $100 M_{\odot} \text{ yr}^{-1}$ at $z = 6$. They both have SFR–stellar mass relation consistent with observations, and a specific SFR of $\simeq 5 \text{ Gyr}^{-1}$. The main differences arise in the gas properties. The non-equilibrium chemistry determines the H \rightarrow H₂ transition to occur at densities $> 300 \text{ cm}^{-3}$, i.e. about 10 times larger than predicted by the equilibrium model used for Dahlia. As a result, Althæa features a more clumpy and fragmented morphology, in turn making SN feedback more effective. Also, because of the lower density and weaker feedback, Dahlia sits 3σ away from the Schmidt-Kennicutt relation; Althæa, instead nicely agrees with observations. The different gas properties result in widely different observables. Althæa outshines Dahlia by a factor of 7 (15) in [C II] $157.74 \mu\text{m}$ (H₂ $17.03 \mu\text{m}$) line emission. Yet, Althæa is under-luminous with respect to the locally observed [C II]–SFR relation. Whether this relation does not apply at high- z or the line luminosity is reduced by CMB and metallicity effects remains as an open question.

Key words: galaxies: high-redshift, formation, evolution, ISM – infrared: general – methods: numerical

1 INTRODUCTION

Understanding the properties of the interstellar medium (ISM) of primeval galaxies is a fundamental challenge of physical cosmology. The high sensitivity/spatial resolution allowed by current observations have dramatically improved our understanding of the ISM of local and moderate redshift ($z = 2 - 3$) galaxies (Osterbrock 1989; Stasińska 2007; Pérez-Montero 2017; Stanway 2017). We now have a clearer picture of the gas phases and thermodynamics (Daddi et al. 2010a; Carilli & Walter 2013), particularly for what concerns

the molecular component, representing the stellar birth environment (Klessen & Glover 2014; Krumholz 2015).

For galaxies located in the Epoch of Reionization (EoR, $5 \lesssim z \lesssim 15$) optical/near infrared (IR) surveys have been very successful in their identification and characterization in terms of stellar mass and star formation rate (Dunlop 2013; Madau & Dickinson 2014; Bouwens et al. 2015). However, only recently we have started to probe the internal structure of such objects. With the advent of the Atacama Large Millimeter/Submillimeter Array (ALMA) it is now possible to access the far infrared (FIR) band at high- z with an unprecedented resolution and sensitivity. Excitingly, this en-

* andrea.pallottini@centrofermi.it; ap926@mrao.cam.ac.uk

ables for the first time studies of ISM energetics, structure and composition in such pristine objects.

Since C II is one of the major coolant of the ISM, [C II] ALMA detections (and upper limits) have so far mostly used this line for the above purposes (Maiolino et al. 2015; Willott et al. 2015; Capak et al. 2015) and to determine the sizes of early galaxies (Fujimoto et al. 2017). Line emission from different species (e.g. [O III]) have been used to derive the interstellar radiation field (ISRF) intensity (Inoue et al. 2016; Carniani et al. 2017), while continuum detections give us a measure of the dust content and properties (Watson et al. 2015; Laporte et al. 2017). Finally, some observations are beginning to resolve different ISM components and their dynamics by detecting spatial offsets and kinematic shifts between different emission lines, i.e. [C II] and optical-ultraviolet (UV) emission (Maiolino et al. 2015; Capak et al. 2015), [C II] and Ly α (Pentericci et al. 2016; Bradac et al. 2017) and [C II] and [O III] (Carniani et al. 2017).

In spite of these progresses, several pressing questions remain unanswered. A partial list includes: (a) What is the chemical composition and thermodynamic state of the ISM in high- z galaxies? (b) How does the molecular gas turns into stars and regulate the evolution of these systems? (c) What are the optimal observational strategies to better constrain the properties of these primeval objects?

Theoretically, cosmological numerical simulations have been used to attack some of these problems. The key idea is to produce a coherent physical framework within which the observed properties can be understood. Such learning strategy is also of fundamental importance to devise efficient observations from current (e.g. HST/ALMA), planned (JWST) and proposed (SPICA) instruments. Before this strategy can be implemented, though, it is necessary to develop reliable numerical schemes catching all the relevant physical processes. While the overall performances of the most widely used schemes have been extensively benchmarked (Scannapieco et al. 2012; Kim et al. 2014, 2016), high-resolution simulations of galaxy formation introduce a new challenge: they are very sensitive to the implemented physical models, particularly those acting on small scales.

Among these, the role of feedback, i.e. how stars affect their own formation history via energy injection in the surrounding gas by supernova (SN) explosions, stellar winds and radiation, is far from being completely understood, despite considerable efforts to improve its modeling (Agertz & Kravtsov 2015; Martizzi et al. 2015) and understand its consequences on high- z galaxy evolution (Ceverino et al. 2014; O’Shea et al. 2015; Barai et al. 2015; Pallottini et al. 2017; Fiacconi et al. 2017; Hopkins et al. 2017).

Additionally, we are still lacking a completely self-consistent treatment of radiation transfer. This is an area in which intensive work is ongoing in terms of faster numerical schemes (Wise et al. 2012; Rosdahl et al. 2015; Katz et al. 2016), or improved physical modelling (Petkova & Maio 2012; Roskar et al. 2014; Maio et al. 2016).

A third aspect has received comparatively less attention so far in high- z galaxy formation studies, i.e. the implementation of adequate chemical networks. While various models have been proposed and tested (Krumholz et al. 2009; Bovino et al. 2016; Grassi et al. 2017), the galaxy-scale consequences of the different prescriptions are still largely unex-

plored (Tomassetti et al. 2015; Maio & Tescari 2015; Smith et al. 2017). Besides, there is no clear consensus on a minimal set of physical ingredients required to produce reliable simulations.

The purpose of this paper is to analyze the impact of H₂ chemistry on the internal structure of high- z galaxies. To this aim, we simulate two prototypical $M_\star \simeq 10^{10} M_\odot$ Lyman Break Galaxies (LBG) at $z = 6$, named “Dahlia” and “Althæa”, respectively. The two simulations differ for the H₂ formation implementation, equilibrium vs. non-equilibrium. We show how chemistry has a strong impact on the observed properties of early galaxies.

The paper is organized as follows. In Sec. 2 we describe the two simulations highlighting common features (Sec. 2.1), separately discussing the different chemical models used for Dahlia (Sec. 2.2) and Althæa (Sec. 2.3). Results are presented as follow. First we perform a benchmark of the chemical models (Sec. 2.4), and compare the star formation and feedback history of the two galaxies (Sec. 3.1). Next, we characterize their differences in terms of morphology (Sec. 3.2), thermodynamical state of the ISM (Sec. 3.3), and predicted [C II] and H₂ (Sec. 4) emission line properties. Our conclusions are summarized in Sec. 5.

2 NUMERICAL SIMULATIONS

To assess the impact of H₂ chemistry on the internal structure of high- z galaxies, we compare two zoom-in simulations adopting different chemical models. Both simulations follow the evolution of a prototypical $z = 6$ LBG galaxy hosted by a $M_h \simeq 10^{11} M_\odot$ dark matter (DM) halo (virial radius $r_{\text{vir}} \simeq 15$ kpc).

The first simulation has been presented in Pallottini et al. (2017, hereafter P17). The targeted galaxy (which includes also about 10 satellites) is called “Dahlia” (see also Gallerani et al. 2016, for analysis of its infall/outflow structure). In such previous work we showed that Dahlia’s specific SFR (sSFR) is in agreement with both analytical calculations (Behroozi et al. 2013), and with $z = 7$ observations (González et al. 2010, see also Sec. 3.1).

In the second, new simulation we follow the evolution of “Althæa”, by using improved thermo-chemistry, but keeping everything else (initial conditions, resolution, star formation and feedback prescriptions) unchanged with respect to the Dahlia simulation. We describe the implementation of these common processes in the following Section. Next we describe separately the chemical model used for Dahlia (Sec. 2.2) and Althæa (Sec. 2.3).

2.1 Common physical models

Both simulations are performed with a customized version of the Adaptive Mesh Refinement (AMR) code RAMSES (Teyssier 2002). Starting from cosmological IC¹ generated

¹ We assume cosmological parameters compatible with *Planck* results: Λ CDM model with total matter, vacuum and baryonic densities in units of the critical density $\Omega_\Lambda = 0.692$, $\Omega_m = 0.308$, $\Omega_b = 0.0481$, Hubble constant $H_0 = 100 \text{ h km s}^{-1} \text{ Mpc}^{-1}$ with $h = 0.678$, spectral index $n = 0.967$, $\sigma_8 = 0.826$ (Planck Collaboration et al. 2014).

with MUSIC (Hahn & Abel 2011), we zoom-in the $z \simeq 6$ DM halo hosting the targeted galaxy. The total simulation volume is $(20 \text{ Mpc}/h)^3$ that is evolved with a base grid with 8 levels (gas mass $6 \times 10^6 M_\odot$); the zoom-in region has a volume of $(2.1 \text{ Mpc}/h)^3$ and is resolved with 3 additional level of refinement, thus yielding a gas mass resolution of $m_b = 1.2 \times 10^4 M_\odot$. In such region, we allow for 6 additional level of refinement, that allow to follow the evolution of the gas down to scales of $l_{\text{cell}} \simeq 30 \text{ pc}$ at $z = 6$, i.e. the refined cells have mass and size typical of Galactic molecular clouds (MC, e.g. Federrath & Klessen 2013). The refinement is performed with a Lagrangian mass threshold-based criterion, i.e. a cell is refined if its total (DM+baryonic) mass exceed the the mass resolution by a factor 8.

Metallicity (Z) is followed as the sum of heavy elements, assumed to have solar abundance ratios (Asplund et al. 2009). We impose an initial metallicity floor $Z_{\text{floor}} = 10^{-3} Z_\odot$ since at $z \gtrsim 40$ our resolution is still insufficient to catch the metal enrichment by the first stars (e.g. O’Shea et al. 2015). Such floor is compatible with the metallicity found at high- z in cosmological simulations for diffuse enriched gas (Davé et al. 2011; Pallottini et al. 2014a; Maio & Tescari 2015); it only marginally affects the gas cooling time.

Dust evolution is not explicitly tracked during simulations. However, we make the simple assumption that the dust-to-gas mass ratio scales with metallicity, i.e. $\mathcal{D} = \mathcal{D}_\odot (Z/Z_\odot)$, where $\mathcal{D}_\odot/Z_\odot = 0.3$ for the Milky Way (MW, e.g. Hirashita & Ferrara 2002; Asano et al. 2013).

2.1.1 Star formation

Stars form according to a linearly H_2 -dependent Schmidt-Kennicutt relation (Schmidt 1959; Kennicutt 1998) i.e.

$$\dot{\rho}_* = \zeta_{\text{sf}} f_{\text{H}_2} \frac{\rho}{t_{\text{ff}}}, \quad (1)$$

where $\dot{\rho}_*$ is the local SF rate density, ζ_{sf} the SF efficiency, f_{H_2} the H_2 mass fraction, and $\rho = \mu m_p n$ is density of the gas of mean molecular weight μ . Eq. 1 is solved stochastically, by drawing the mass of the new star particles from a Poisson distribution (Rasera & Teyssier 2006; Dubois & Teyssier 2008; Pallottini et al. 2014a). In detail, in a star formation event we create a star particle with mass Nm_b , with N an integer drawn from

$$P(N) = \frac{\langle N \rangle}{N!} \exp -\langle N \rangle, \quad (2)$$

where the mean of the Poisson distribution is

$$\langle N \rangle = \frac{f_{\text{H}_2} \rho_{\text{cell}}^3 \zeta_{\text{sf}} \delta t}{m_b t_{\text{ff}}}, \quad (3)$$

with δt the simulation time step. For numerical stability, no more than half of the cell mass is allowed to turn into stars. Since we prevent formation of star particle with mass less than m_b , cells with density less than $\sim 15 \text{ cm}^{-3}$ (for $l_{\text{cell}} \simeq 30 \text{ pc}$) are not allowed to form stars.

We set $\zeta_{\text{sf}} = 0.1$, in accordance with the average values inferred from MC observations (Murray 2011, see also Agertz et al. 2013); f_{H_2} depends on the adopted thermochemical model, as described later in Sec. 2.2 and Sec. 2.3.

2.1.2 Feedback

Similarly to Kim et al. (2014), we account for stellar energy inputs and chemical yields that depend both on time and stellar populations by using STARBURST99 (Leitherer et al. 1999). Stellar tracks are taken from the padova (Bertelli et al. 1994) library with stellar metallicities in the range $0.02 \leq Z_*/Z_\odot \leq 1$, and we assume a Kroupa (2001) initial mass function. Stellar feedback includes SNe, winds from massive stars and radiation pressure (Agertz et al. 2013). We model the thermal and turbulent energy content of the gas according to the prescriptions by Agertz & Kravtsov (2015). The turbulent (or non-thermal) energy is dissipated as $\dot{e}_{\text{nth}} = -e_{\text{nth}}/t_{\text{diss}}$ (Teyssier et al. 2013, see eq. 2), where, following Mac Low (1999), the dissipation time scale can be written as

$$t_{\text{diss}} = 9.785 \left(\frac{l_{\text{cell}}}{100 \text{ pc}} \right) \left(\frac{\sigma_{\text{turb}}}{10 \text{ km s}^{-1}} \right)^{-1} \text{ Myr}, \quad (4)$$

where σ_{turb} is the turbulent velocity dispersion. Adopting the SN blastwave models and OB/AGB stellar winds from Ostriker & McKee (1988) and Weaver et al. (1977), respectively, we account for the dissipation of energy in MCs as detailed in Sec. 2.4 and App. A of P17.

2.2 Dahlia: equilibrium thermo-chemistry

In the Dahlia simulation we compute f_{H_2} by adopting the KTM09 analytical prescription (Krumholz et al. 2008, 2009; McKee & Krumholz 2010). In KTM09, the H_2 abundance is derived by modelling the radiative transfer on an idealized MC and by assuming equilibrium between H_2 formation on dust grains and dissociation rates. For each gas cell, f_{H_2} can then be written as a function of n , Z and hydrogen column density (N_{H}). By further assuming pressure equilibrium between CNM and WNM (Krumholz et al. 2009), f_{H_2} turns out to be independent on the intensity of the ISRF, and can be written as

$$f_{\text{H}_2} = [1 - 0.75 s / (1 + 0.25 s)] \Theta(2 - s), \quad (5a)$$

with

$$s = \ln(1 + 0.6 \chi + 0.01 \chi^2) / (0.6 \tau_{\text{UV}}) \quad (5b)$$

$$\chi = 0.75 [1 + 3.1 (Z/Z_\odot)^{0.365}], \quad (5c)$$

and where Θ is the Heaviside function; τ_{UV} is the dust UV optical depth and it can be calculated by linearly rescaling the MW value,

$$\tau_{\text{UV}} = \left(\frac{N_{\text{H}}}{1.6 \times 10^{21} \text{ cm}^{-2}} \right) \left(\frac{\mathcal{D}}{\mathcal{D}_\odot} \right). \quad (6)$$

In Dahlia cooling/heating rates are computed using GRACKLE 2.1² (Bryan et al. 2014). We use a H and He primordial network, and tabulated metal cooling/photo-heating rates from CLOUDY (Ferland et al. 2013). Inverse Compton cooling is also present, and we consider heating from a redshift-dependent ionizing UV background (UVB, Haardt & Madau 2012). Since H_2 is not explicitly included in the network, we do not include the corresponding cooling contribution.

² <https://grackle.readthedocs.org/>

2.3 Althæa: non-equilibrium thermo-chemistry

In Althæa we implement a non-equilibrium chemical network by using KROME³ (Grassi et al. 2014). Given a set of species and their reactions, KROME can generate the code needed to solve the system of coupled ordinary differential equations that describe the gas thermo-chemical evolution.

2.3.1 Chemical network

Similarly to Bovino et al. (2016, hereafter B16), our network includes H, H⁺, H⁻, He, He⁺, He⁺⁺, H₂, H₂⁺ and electrons. Metal species are not followed individually in the network, as for instance done in Model IV from B16; therefore, we use an equilibrium metal line cooling calculated via CLOUDY tables⁴. The adopted network contains a total of 37 reactions, including photo-chemistry (Sec. 2.3.2), dust processes (Sec. 2.3.3) and cosmic rays (CR, Sec. 2.3.4). The reactions, their rates, and corresponding references are listed in App. B of B16: specifically we use reactions from 1 to 31 (Tab. B.1 in B16), 53, 54, and from 58 to 61 (Tab. B.2 in B16).

2.3.2 Photo-chemistry

Photo-chemistry cross sections are taken from Verner & Ferland (1996) and by using the SWRI⁵ and Leiden⁶ databases. In the present simulation, the ISRF is not evolved self-consistently and it is approximated as follows. For the spectral energy density (SED), we assume a MW like spectrum (Black 1987; Draine 1978), and we specify the SED using 10 energy bins from 0.75 eV to 14.16 eV. Beyond 13.6 eV the flux drops to zero, i.e. we do not include ionizing radiation.

We consider a spatially uniform ISRF whose intensity is rescaled with the SFR such that $G = G_0(\text{SFR}/M_\odot \text{ yr}^{-1})$, where $G_0 = 1.6 \times 10^{-3} \text{ erg cm}^{-2} \text{ s}^{-1}$ is the far UV (FUV) flux in the Habing band (6 – 13.6 eV) normalized to the average MW value (Habing 1968). Because of their sub-kpc sizes (Shibuya et al. 2015, Fujimoto et al. 2017) high G_0 values are expected in typical LBG at $z \simeq 6$, as inferred also by Carniani et al. (2017). A similar situation is seen in some local dwarf galaxies (Cormier et al. 2015) that are generally considered as local counterparts of high- z galaxies. It is worth noting that the spatial variation of G is very small in the MW, with an r.m.s. value $\simeq 3 G_0$ (Habing 1968; Wolfire et al. 2003). Nonetheless, spatial fluctuations of the ISRF, if present, might play some role in the evolution of high- z galaxies (e.g. Katz et al. 2016). We will analyze this effect in future work.

³ <https://bitbucket.org/tgrassi/krome>

⁴ As a caveat, we point out that there is a formal inconsistency in the modelling. Metal line cooling tables are usually calculated with CLOUDY by assuming a Haardt & Madau (2012) UV background, while the ISRF spectral energy density we adopt is MW-like. To remove such inconsistency one should explicitly track metal species, adopt a non-equilibrium metal line cooling and include radiative transfer. As noted in B16 (see their Fig. 16), using non-equilibrium metal line cooling can typically change the cooling function by a factor $\lesssim 2$. This will be addressed in future work.

⁵ <http://phidrates.space.swri.edu>

⁶ <http://home.strw.leidenuniv.nl/~ewine/photo/>

On top of the ISRF, we consider the cosmic microwave background (CMB), that effectively sets a temperature floor for the gas. Additionally, we neglect the cosmic UVB, since the typical ISM densities are sufficiently large to ensure an efficient self-shielding (e.g. Gnedin 2010). For example, Rahmati et al. (2013) have shown that at $z \simeq 5$ the hydrogen ionization due to the UVB is negligible for $n \gtrsim 10^{-2} \text{ cm}^{-3}$, the typical density of diffuse ISM. The self-shielding of H₂ to photo-dissociation is accounted by using the Richings et al. (2014) prescription⁷, thus in each gas cell the shielding can be expressed as an analytical function of its H₂ column density, temperature and turbulence (cfr. with Wolcott-Green et al. 2011).

2.3.3 Dust processes

As for Dahlia, the dust mass is proportional to the metal mass. Here we also specify the dust size distribution to be the one appropriate for high- z galaxies, the Small Magellanic Cloud one, following Weingartner & Draine (2001). Dust grains can affect the chemistry through cooling⁸ (Hollenbach & McKee 1979), photoelectric-heating (Bakes & Tielens 1994), and by mediating the formation of molecules (Cazaux & Spaans 2009). In particular, the formation rate of H₂ on dust grains is approximated following Jura (1975)

$$R_{\text{H}_2-\text{dust}} = 3 \times 10^{-17} n_{\text{H}} (\mathcal{D}/\mathcal{D}_\odot) \text{ cm}^{-3} \text{ s}^{-1}, \quad (7)$$

where n_{H} is the hydrogen density. Note that for $\mathcal{D} \gtrsim 10^{-2} \mathcal{D}_\odot$ this dust channel is dominant with respect to gas-phase formation (e.g. reactions 6–7 and 9–10 B.1 in B16).

2.3.4 Cosmic rays

CR ionization can become important in regions shielded from radiation, like MC interiors. We assume a CR hydrogen ionization rate \propto SFR (Valle et al. 2002) and normalized to the MW value (Webber 1998):

$$\zeta_{\text{cr}} = 3 \times 10^{-17} (\text{SFR}/M_\odot \text{ yr}^{-1}) \text{ s}^{-1}. \quad (8)$$

The rate ζ_{cr} includes the flux of CR and secondary electrons (Richings et al. 2014). In the network, CR ionizations are proportional to ζ_{cr} and to coupling constants that depend on the specific ions; such couplings are taken from the KIDA database (Wakelam et al. 2012). Additionally we account for Coulomb heating, by assuming that every CR ionization releases an energy⁹ of 20 eV.

2.3.5 Initial abundances of the species

Finally, following Galli & Palla (1998), we calculate IC for the various species by accounting for the primordial chem-

⁷ The self-shielding formulation by Richings et al. (2014) does not account for a directional dependence as done in more computationally costly models (Hartwig et al. 2015).

⁸ Dust cooling is not included in the current model, as it gives only a minor contribution for $n < 10^4 \text{ cm}^{-3}$, i.e. see Fig. 3 in B16.

⁹ For a more accurate treatment of Coulomb heating refer to Glassgold et al. (2012).

istry¹⁰ at $z \gtrsim 100$, for a density and temperature evolution corresponding to gas at the mean cosmic density.

2.4 Benchmark of H₂ formation models

As a benchmark for our simulations, we compare the formation of H₂ in different physical environments. For the Dahlia KTM09 model we compute f_{H_2} from eq. 5 as a function of n and Z . We choose an expression for $N_{\text{H}} = n l_{\text{cell}} \mu \propto n^{2/3}$ resulting from the mass threshold-based AMR refinement criterion for which $l_{\text{cell}} \propto n^{-1/3}$. We restate that the equilibrium KTM09 model is independent on G and the gas temperature T .

For the Althæa B16 model we use KROME to perform single-zone tests varying n, Z and G . In this case we assume an initial temperature¹¹ $T = 5 \times 10^3 \text{K}$, and we let the gas patch evolve at constant density until thermo-chemical equilibrium is reached. This typically takes 100 Myr.

The comparison between the two models is shown in Fig. 1 as a function of n for different metallicities. For $G > 0$ and $Z < Z_{\odot}$, H₂ formation is hindered in B16 with respect to KTM09, i.e. higher n are needed to reach similar f_{H_2} fractions. For $G = G_0$ and $Z = Z_{\odot}$ the two models are roughly in agreement: this is expected since KTM09 is calibrated on the MW environment. Finally, for $G > 0$ and at $Z = 10^{-3} Z_{\odot}$ (the metallicity floor in our simulation set) the H₂ formation in the B16 model is strongly suppressed, e.g. $f_{\text{H}_2} \simeq 10^{-3}$ for $n \simeq 10^3 \text{cm}^{-3}$. Note that these fractions are comparable to the ones expected for H₂ formation in a pristine environment where H₂ formation proceeds via gas-phase reactions.

As noted in P17, Dahlia’s star formation (SF) model (eqs 1 and 5) is roughly equivalent to a density threshold criterion with metallicity-dependent critical density $n_c \simeq 26.45 (Z/Z_{\odot})^{-0.87} \text{cm}^{-3}$. Physically this corresponds to the density at which $f_{\text{H}_2} \geq 0.5$ (see also Agertz et al. 2013). Thus, Fig. 1 quantifies the density threshold required to spawn stars in the simulation.

Dahlia forms stars in gas with $n \simeq 30 \text{cm}^{-3}$ and $Z \simeq 0.5 Z_{\odot}$ at a rate of about $10^2 M_{\odot} \text{yr}^{-1}$ at $z = 6$. If Althæa has a similar SFR history (this is checked a posteriori, see Fig. 2), the resulting metallicity and ISRF intensity ($G \simeq 10^2 G_0$) should also be similar. Then, by inspecting Fig. 1 (middle-left panel) one can conclude that Althæa forms stars in much denser environments where $n > n_c \simeq 263 (Z/Z_{\odot})^{-1.19} \text{cm}^{-3}$ for $G = 10^2 G_0$. As noted in Hopkins et al. (2013), although variations in the density threshold lead to similar total SFR, they might severely affect the galaxy morphology. We will return to this point in the next Section.

We remind that in both simulation we use the cell radius to calculate column density, that are used e.g. to calculate the gas self-shielding. This is done to ensure a fair comparison between the two simulations. In other simulations, e.g. MC illuminated by an external radiation

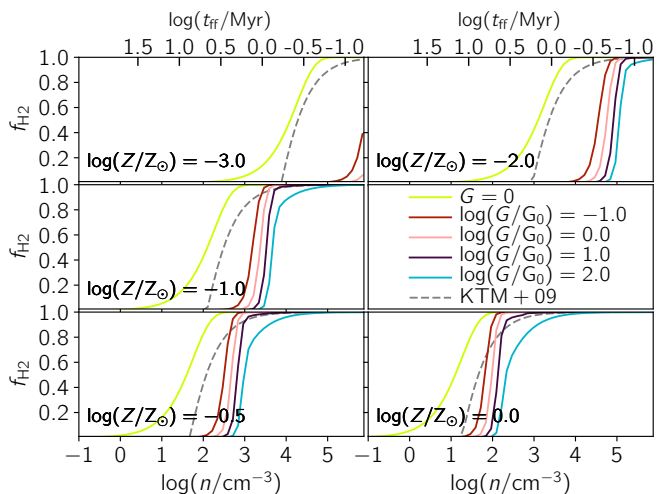


Figure 1. Benchmark of the formation of H₂ for the model used in Dahlia (KTM09, Sec. 2.2) and in Althæa (B16, Sec. 2.3). In each panel we plot the H₂ mass fraction f_{H_2} as a function of density (n), with different panels showing the results for different metallicities (Z). In each panels the dashed grey line indicates the KTM09 model, while the B16 models are plotted with solid lines, with different colours indicating a different impinging ISRF flux (G). In the upper axis we indicate the free-fall times (t_{ff}) corresponding to n .

field, the prescriptions adopted accounts for the contribution of column density from nearby cells, i.e. by using Jeans or Sobolev-like length (see e.g. Hartwig et al. 2015 for a comparison between different prescriptions). However in our simulation we expect stars to be very close or embedded in potential star forming regions. Using the contribution to the column density from the surrounding gas would then overestimate the self-shielding effect. Such modelling uncertainty would be solved by including radiative transfer in the simulation. However, we note that at $z=6$ the radius of our cells as a function of density can be approximated as $r_{\text{cell}} = 154.1 (n/\text{cm}^{-3})^{-1/3} \text{pc}$, while the jeans length is $l_J = 15.6 (n/\text{cm}^{-3})^{-1/2} (T/\text{K})^{1/2} \text{pc}$. Thus for typical values found for the molecular gas in Althæa ($n \simeq 300 \text{cm}^{-3}$ and $T \simeq 100 \text{K}$, see later Fig. 8), the two prescriptions gives similar results, i.e. $r_{\text{cell}} \sim 20 \text{pc}$ and $l_J \sim 10 \text{pc}$.

3 RESULTS

We now turn to a detailed analysis of the two zoomed galaxies, Dahlia and Althæa¹². We start by studying the star formation and the build-up of the stellar mass from $z \simeq 15$ to $z = 6$ (Sec. 3.1). We then specialize at $z = 6$ to inspect the galaxy morphology (Sec. 3.2), the ISM multiphase structure (Sec. 3.3) and the predicted observable properties (Sec. 4). An overall summary of the properties of the two galaxies is given in Tab. 1.

¹² We refrain from the analysis of the satellite population of the two galaxies due to the oversimplifying assumption of a spatially uniform ISRF artificially suppressing star formation in environments with metallicity close to the floor value $Z_{\text{floor}} = 10^{-3} Z_{\odot}$.

¹⁰ For a possible implementation of the Galli & Palla (1998) chemical network see the “earlyUniverse” test contained in KROME.

¹¹ The initial temperature corresponds to the virial temperature of the first star-forming halos present in the zoomed region. The results depend very weakly on this assumption.

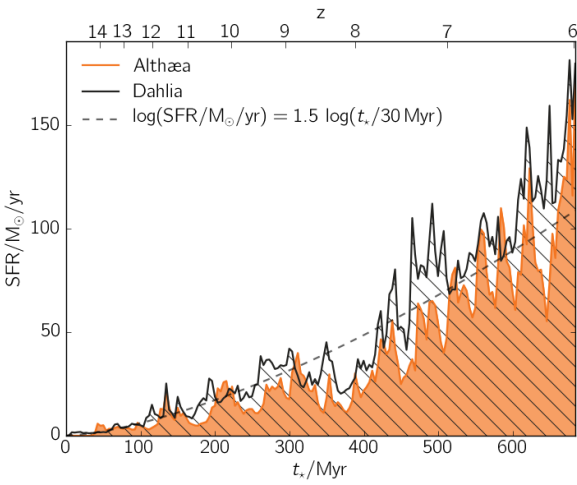


Figure 2. Star formation rate (SFR) as a function of galaxy age (t_*) for Dahlia (black line and hatched region) and Althæa (orange line and transparent region). Also shown (grey dashed line) is an analytical approximation (within a factor 2 for both galaxies) to the average SFR trend. The redshift (z) corresponding to t_* is plotted on the upper axis, and note that $t_* = 0$ corresponds to the first stellar formation event in Dahlia, and the plotted SFRs are averaged over 4 Myr.

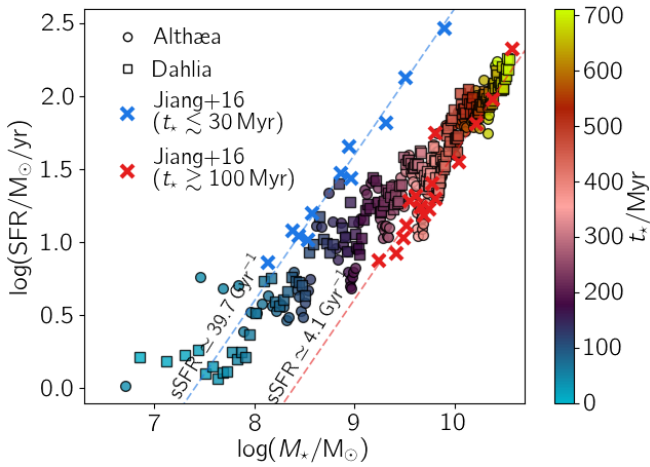


Figure 3. SFR vs stellar mass (M_*) for Althæa (circles) and Dahlia (squares), with symbols coloured accordingly to the age t_* . With crosses we overplot SFR and M_* inferred from 27 galaxies observed at $z \simeq 6$ by J16. Following J16 analysis¹⁴, galaxies identified as young and old are plotted in blue and red, respectively. To guide the eye, the linear correlation between the data sets are also shown with a dashed lines. See the text for more details.

3.1 Star formation history

In Fig. 2 we plot the SFR history as a function of “galaxy age” (t_*) for Dahlia and Althæa; $t_* = 0$ marks the first star formation event in Dahlia¹³. For both Dahlia and Al-

¹³ Note that even with the same modelling and IC, differences in the SFR may arise as a result of stochasticity in the star formation prescription eq. 1. Such differences vanish once the SFR

thæa the SFR has an increasing trend which can be approximated with good accuracy (within a factor of 2) as $\text{SFR} = 1.5 \log(t_*/(30 \text{ Myr}))$. However, on average the SFR in Dahlia is larger by a factor $\simeq 1.5 \pm 0.6$ when averaged over the entire SFR history ($\simeq 700 \text{ Myr}$). Thus, in spite of very different chemical prescriptions, the SFR in the two galaxies shows very little variation. Stated differently, the higher critical density for star formation arising from non-equilibrium chemistry does not alter significantly the rate at which stars form, as already noticed in Sec. 2.4. This also entails a comparable metallicity, and we note that in both galaxy most of the metal mass is locked in stars (see Tab. 1), as they are typically formed from the most enriched regions.

It is interesting to check the evolutionary paths of Dahlia and Althæa (Fig. 3) in the standard SFR vs. stellar mass (M_*) diagram, and compare them with data¹⁴ inferred from $z \simeq 6$ observations of 27 Lyman Alpha Emitters (LAE) and LBGs (Jiang et al. 2016, hereafter J16). By using multi-band data, precise redshift determinations, and an estimate of nebular emission from Ly α , J16 were able to distinguish between a young ($t_* \lesssim 30 \text{ Myr}$) and an old ($t_* \gtrsim 100 \text{ Myr}$) subsample. Each subsample exhibits a linear correlation in $\log \text{SFR} - \log M_*$, albeit with a different normalization: the young (old) subsample has a $\text{sSFR} = \text{SFR}/M_* = 39.7 \text{ Gyr}^{-1} (4.1 \text{ Gyr}^{-1})$.

The SFR vs stellar mass of our simulated galaxies for $M_* \lesssim 10^{8.5} M_\odot$ ($t_* \lesssim 100 \text{ Myr}$) is fairly consistent with the young subsample relation (keeping in mind stochasticity effects at low stellar masses). At later evolutionary stages ($t_* \gtrsim 300 \text{ Myr}$ or $M_* \gtrsim 10^{9.5} M_\odot$), Dahlia and Althæa nicely shift to the lower sSFR values characterizing the old J16 subsample data. This shift must be understood as a result of increasing stellar feedback: as galaxies grow, the larger energy input from the accumulated stellar populations hinders subsequent SFR events. Note that at late times ($t_* \gtrsim 300 \text{ Myr}$), when $M_* = 5 \times 10^9 M_\odot$, the sSFRs of Dahlia and Althæa are in agreement with analytical results by Behroozi et al. (2013), and with $z = 7$ observations by González et al. (2010).

As feedback clearly plays a major role in the overall evolution of early galaxies, we turn to a more in-depth analysis of its energetics. This can be quantified in terms of the stellar energy deposition rates in *mechanical* (SN explosions + OB/AGB winds¹⁵, $\dot{E}_{\text{sn+w}}$) and *radiative* (\dot{E}_{rad}) forms. These are shown as a function of time in Fig. 4. The $\dot{E}_{\text{sn+w}}/\dot{E}_{\text{rad}}$ ratio shows short-term ($\simeq 20 \text{ Myr}$) fluctuations corresponding to coherent burst of star formation/SN activity.

Barring this time modulation, on average the mechanical/radiative energy ratio increases up to $\simeq 250 \text{ Myr}$, when it suddenly drops and reaches an equilibrium value. This implies that radiation pressure dominates the energy input; consequently it represents the major factor in quenching star formation. While this is true throughout the evolution, it becomes even more evident after $\simeq 250 \text{ Myr}$, when the first

is averaged on timescales longer than the typical free-fall time of the star forming gas.

¹⁴ SFR and M_* have been derived by assuming an exponentially increasing SFR, consistent with the history of both our simulated galaxies (Fig. 2).

¹⁵ On average OB/AGB winds account only for $\lesssim 10\%$ of the SN power.

Property	Symbol	Dahlia	Althæa	[units]
Star formation rate	SFR	156.19	136.50	M_{\odot}/yr
Specific SFR	sSFR	4.45	5.23	Gyr^{-1}
Stellar mass	M_{\star}	3.51	2.61	$10^{10}M_{\odot}$
Metal mass in stars	M_{\star}^Z	8.20	5.87	10^8M_{\odot}
Gas mass	M_g	1.23	2.72	10^9M_{\odot}
H ₂ mass	M_{H_2}	17.01	4.76	10^7M_{\odot}
Metal mass	M_Z	1.41	2.48	10^7M_{\odot}
Disk radius	r_d	610	504	pc
Disk scale height	H	224	191	pc
Gas density	$\langle n \rangle$	23.89	164.41	cm^{-3}
H ₂ density	$\langle n_{\text{H}_2} \rangle$	6.62	4.95	cm^{-3}
Metallicity	$\langle Z \rangle$	0.57	0.46	Z_{\odot}
Gas surface density	$\langle \Sigma \rangle$	37.89	222.02	M_{\odot}/pc^2
Star formation surface density	$\langle \dot{\Sigma}_{\star} \rangle$	0.40	0.83	$M_{\odot}/\text{pc}^2/\text{Myr}$
Luminosity [C II] 157.74 μm	L_{CII}	3.39	21.08	10^7L_{\odot}
Luminosity H ₂ 17.03 μm	L_{H_2}	2.31	33.24	10^8L_{\odot}

Table 1. Physical properties of Dahlia and Althæa at $z = 6$. The values refer to gas and stars within 2.5 kpc from the galaxy center (similar to the field of view in Figs 5 and 11). The effective radius, r_d , and gas scale height, H , are calculated from the principal component analysis of the density field. Values for n , n_{H_2} , Z , Σ , and $\dot{\Sigma}_{\star}$ represent mass-weighted averages.

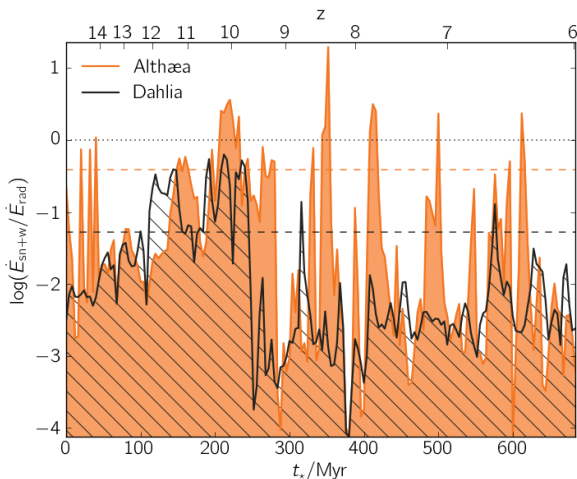


Figure 4. Ratio of mechanical ($\dot{E}_{\text{sn}+\text{w}}$) and radiative (\dot{E}_{rad}) energy deposition rates by stars as a function of galaxy age (t_{\star}) for Dahlia (black line/hatched area) and Althæa (orange/transparent). Dashed lines indicate the $\simeq 700$ Myr time-averaged mean of the ratios for each galaxy. To guide the eye we plot the unity value (dotted grey line). Similar to Fig. 2 the ratios are averaged over 4 Myr. The upper horizontal axis indicates redshift.

stellar populations with $Z_{\star} \gtrsim 10^{-1}Z_{\odot}$ enter the AGB phase. At that time, winds from AGBs enrich their surroundings with metals and dust. As dust produced by AGBs remains more confined than SN dust around the production region, it provides a higher opacity, thus boosting radiation pressure via a more efficient dust-gas coupling (see also P17).

For Dahlia the radiative energy input rate is about 20 times larger than the mechanical one, while for Althæa such ratio is on average 8 times higher, although larger fluctuations are present. The latter are caused by the occurrence of more frequent and powerful bursts of SN events in Althæa. Why does this happen?

The answer has to do with the different gas morphology. As already noted discussing Fig. 1, the higher critical density for star formation imposed by non-equilibrium chemistry has a number of consequences: (a) each formation event can produce a star cluster with an higher mass; (b) star formation is more likely hosted in isolated high density clumps (see later, particularly Fig. 6); (c) in a clumpier disk, SN explosions can easily break into more diffuse regions. The combination of (a) and (b) increases the probability of spatially coherent explosions having a stronger impact on the surrounding gas; due to (c), the blastwaves suffer highly reduced radiative losses (Gatto et al. 2015), and affect larger volumes. Similar effects have been also noted in the context of single giant MCs ($\sim 10^6M_{\odot}$), where unless the SNe explode coherently, their energy is quickly radiated away because of the very high gas densities (Rey-Raposo et al. 2017). For the remainder of the work we focus on $z = 6$, when the galaxies have an age of $t_{\star} \simeq 700$ Myr.

3.2 Galaxy morphology

Dahlia and Althæa sit at the centre of a cosmic web knot and accrete mass from the intergalactic medium mainly via 3 filaments of length $\simeq 100$ kpc. In both simulations, the large scale structure is similar, and we refer the reader to Sec. 3.1 of P17 for its analysis. Differences between the simulation are expected to arise on the ISM scale, whose structure is visible on $\simeq 7$ kpc scales. In Fig. 5 we show the gas density, temperature, and H₂ density ($n_{\text{H}_2} = f_{\text{H}_2} n_{\mu}$) fields for Dahlia and Althæa. The map¹⁶ centers coincide with Dahlia’s stellar center-of-mass.

¹⁶ The maps of this work are rendered by using a customized version of PYMSES (Labadens et al. 2012), a visualization software that implements optimized techniques for the AMR of RAMSES.

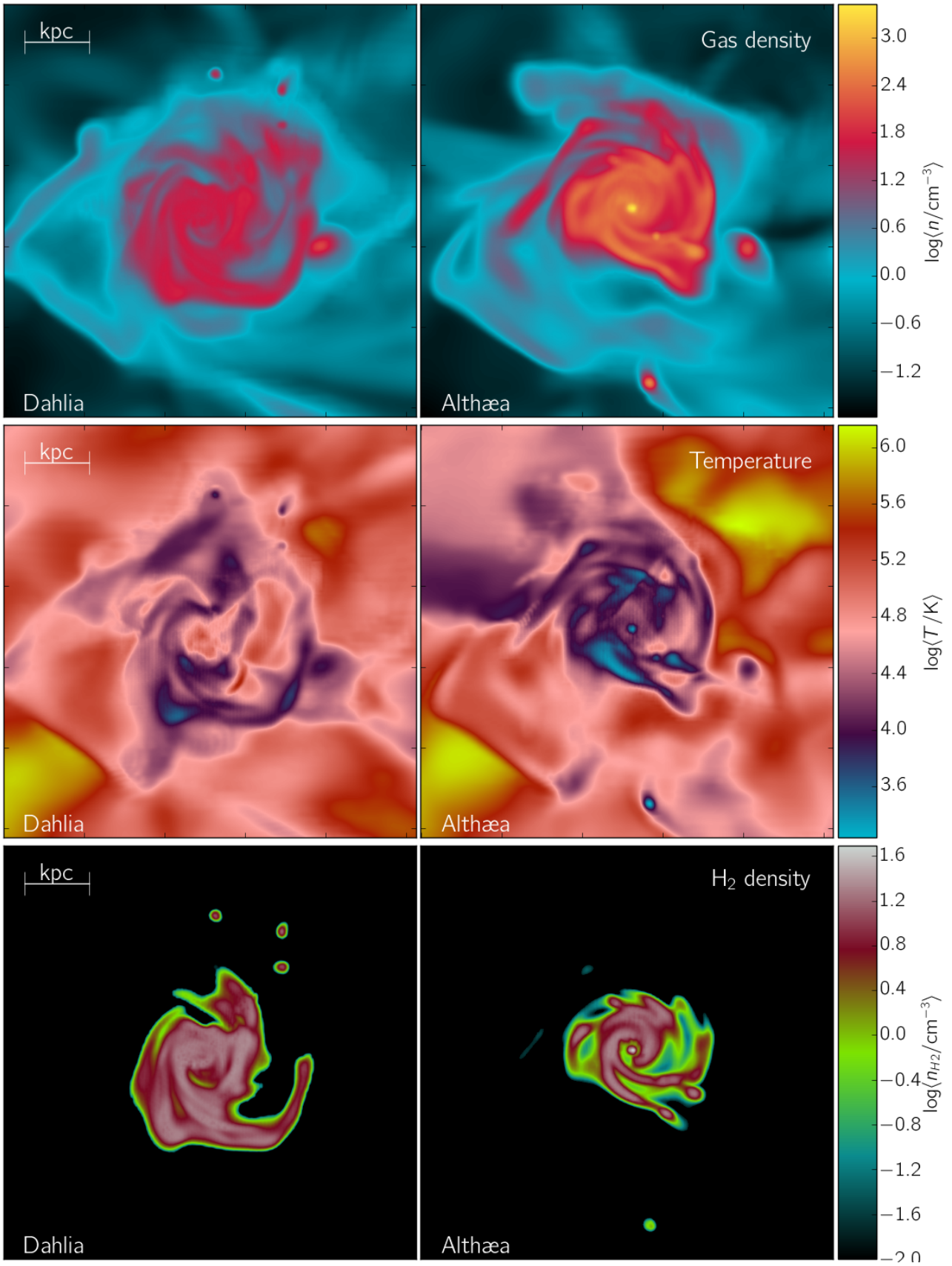


Figure 5. (Caption next page.)

Figure 5. (Previous page.) Face-on maps¹⁶ of Dahlia (left panels) and Althæa (right) at age $t_* \simeq 700$ Myr ($z = 6$). Shown are line-of-sight mass weighted average of the gas density (upper panels), temperature (middle), and H_2 density (lower) fields with amplitude given by the colorbar. The maps are 6.31 kpc on a side.

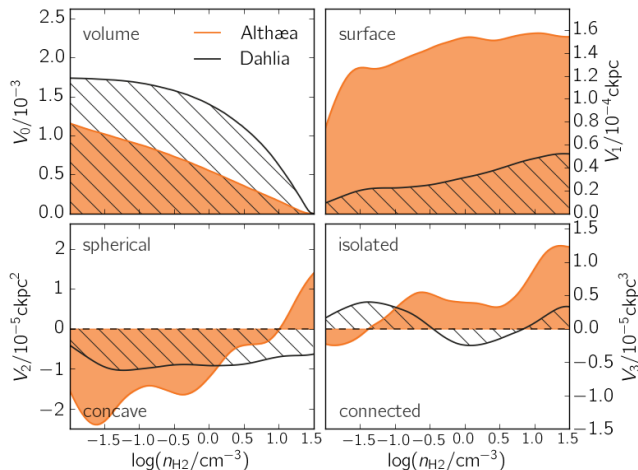


Figure 6. Morphological comparison of the molecular gas at $z = 6$. In the four panels we plot the Minkowsky functionals (V_0, V_1, V_2, V_3) of the H_2 density field ($n_{\text{H}_2}/\text{cm}^{-3}$). Functionals are plotted with black line and hatched regions for Dahlia, with orange line and transparent region for Althæa. Note that Minkowsky functionals are indicated in comoving units. For detail on the calculation of the Minkowsky functional see App. A (in particular see Fig. A1).

3.2.1 Overview

Qualitatively, both galaxies show a clearly defined, albeit somewhat perturbed, spiral disk of radius $\simeq 0.5$ kpc, embedded in a lower density ($n \simeq 0.1 \text{ cm}^{-3}$) medium. However the mean disk gas density for Dahlia is $\langle n \rangle = 24 \text{ cm}^{-3}$, while for Althæa $\langle n \rangle = 164 \text{ cm}^{-3}$ (see Tab. 1). The temperature structure shows fewer differences, i.e. the inner disk is slightly hotter for Dahlia ($T \simeq 300$ K) than for Althæa ($T \simeq 100$ K), which features instead slightly more abundant and extended pockets of shock-heated gas ($T \gtrsim 10^6$). Such high- T regions are produced by both accretion shocks and SN explosions. In both cases the typical H_2 density is the same, i.e. $\langle n_{\text{H}_2} \rangle = 5 \text{ cm}^{-3}$, however, with respect to Dahlia, Althæa shows a slightly smaller disk, that also seems more clumpy.

To summarize, the galaxies differ by an order of magnitude in atomic density, but have the same molecular density. In spite of this difference, the SFR are roughly similar. This can be explained as follows. To first order, in our model $SFR \propto n_{\text{H}_2} n^{1/2} V$, where $V = 2\pi r_d^2 H$ is the galaxy volume (Tab. 1). It follows that the larger density is largely compensated by the smaller Althæa volume.

3.2.2 In-depth analysis

Fig. 5 visually illustrates the morphological differences between the two galaxies. The gas in Althæa appears clumpier than in Dahlia. To quantify this statement we start by introducing the H_2 clumping factor on the smoothing scale r ,

which is defined as¹⁷

$$C(r) = \langle n_{\text{H}_2}^2 \rangle_r / \langle n_{\text{H}_2} \rangle_r^2, \quad (9)$$

For Dahlia $C(r)$ decreases from 10^3 to 10 going from 30 pc to 1 kpc, while for Althæa $C(r)$ is $\gtrsim 2$ times larger on all scales.

A more in-depth analysis can be performed using the Minkowsky functionals (Schmalzing & Gorski 1998; Gleser et al. 2006; Yoshiura et al. 2017, App. A) which can give a complete description of the molecular gas morphological structure. For a 3-dimensional field, 4 independent Minkowsky functionals can be defined. Each of the functionals, $V_i(n_{\text{H}_2})$ ($i = 0, \dots, 3$) characterizes a different morphological property of the excursion set with H_2 density $> n_{\text{H}_2}$: V_0 gives the volume filling factor, V_1 measures the total enclosed surface, V_2 is the mean curvature, quantifying the sphericity/concavity of the set, and V_3 estimates the Euler characteristic (i.e. multiple isolated components vs. a single connected one). Appendix A gives more rigorous definitions with an illustrative application (Fig. A1).

In Fig. 6 we plot the Minkowsky functionals (V_0, V_1, V_2, V_3) calculated for the H_2 density field for Dahlia and Althæa. The V_0 functional analysis shows that Althæa is more compact, i.e. for each n_{H_2} value Dahlia's excursion set volume is larger and it plummets rapidly at large densities. On the other hand, the set surface of Althæa is larger by about a factor of 5, implying that this galaxy is fragmented into multiple, disconnected components. This is confirmed also by Althæa's larger ($10\times$) Euler characteristic measure, V_3 , an indication of the prevalence of isolated structures. This feature becomes more evident towards larger densities, as expected if H_2 is concentrated in molecular clouds¹⁸.

Further, in Dahlia most of the molecular gas resides in connected ($V_3 \lesssim 0$) disk regions, with a concave shape ($V_2 < 0$). For Althæa there is a transition: for $\log(n_{\text{H}_2}/\text{cm}^{-3}) \lesssim 1$ the gas has a concave ($V_2 < 0$), disjointed ($V_3 > 0$), filamentary structure, while for $\log(n_{\text{H}_2}/\text{cm}^{-3}) \gtrsim 1$ the galaxy is composed by spherical clumps ($V_2 > 0$).

3.3 ISM thermodynamics

The thermodynamical state of the ISM can be analyzed by studying the probability distribution function (PDF) of the gas in the density-temperature plane, i.e. the equation of state (EOS). In Fig. 7 we plot the mass-weighted EOS for Dahlia and Althæa at $z = 6$. We include gas within 30 kpc, or $\simeq 2 r_{\text{vir}}$, from the galaxy center.

From the EOS we can see that in both galaxies 70% of the gas is in a photoionized state ($T \sim 10^4$ K), that in Dahlia is

¹⁷ To calculate the clumping factor, first we construct the 3D unigrid cube of the H_2 mass field, then we smooth it with a Gaussian kernel of scale r and finally we calculate the mass-weighted average and variance of the smoothed H_2 density field.

¹⁸ $V_3 > 0$ values at $\log(n_{\text{H}_2}/\text{cm}^{-3}) \simeq 1.2$ in Dahlia are mainly due to the presence of the 3 satellites/clumps outside the disk.

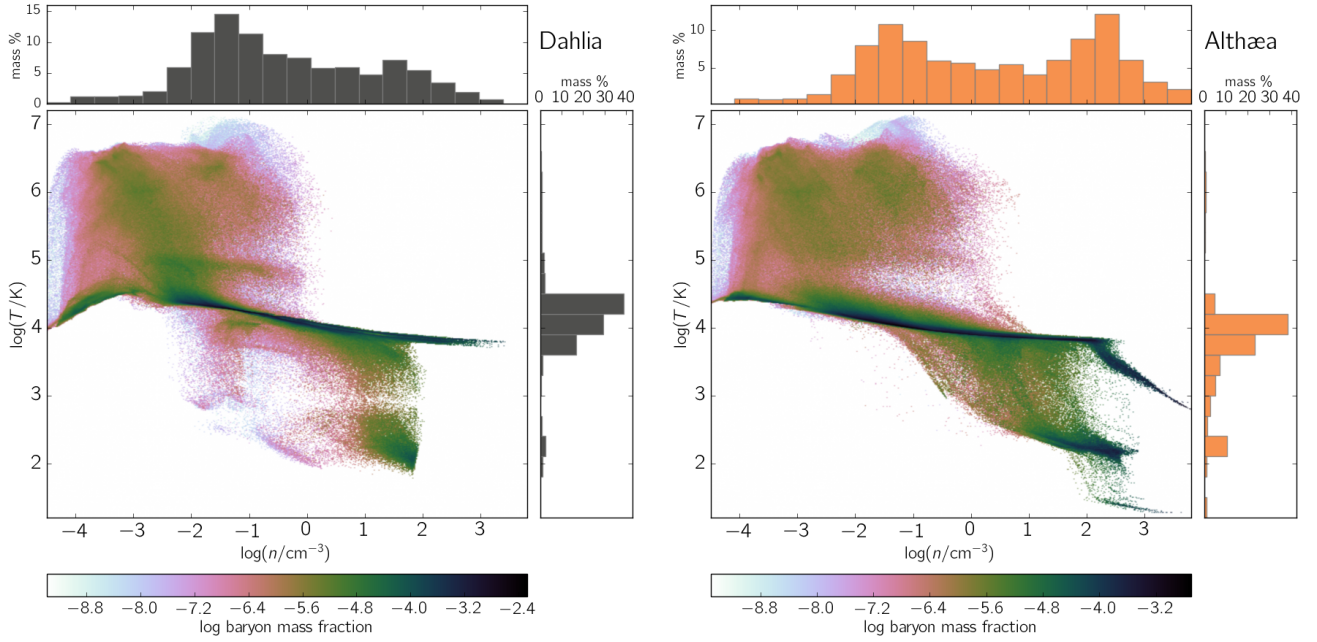


Figure 7. Equation of state (EOS) of the gas within 30 kpc for Dahlia (left panel) and Althæa (right panel) at $t_* \simeq 700$ Myr ($z = 6$). EOS are shown as mass-weighted probability distribution function (PDF) in the density-temperature ($n - T$) plane, as specified by the colorbar. For both galaxies, the EOS projection on the n (T) axis is additionally shown as an horizontal (vertical) inset. The 2D EOS are normalized such that the integral on the $n - T$ plane is unity; the projected EOS are normalized such that the sum of the bins is equal to 100%.

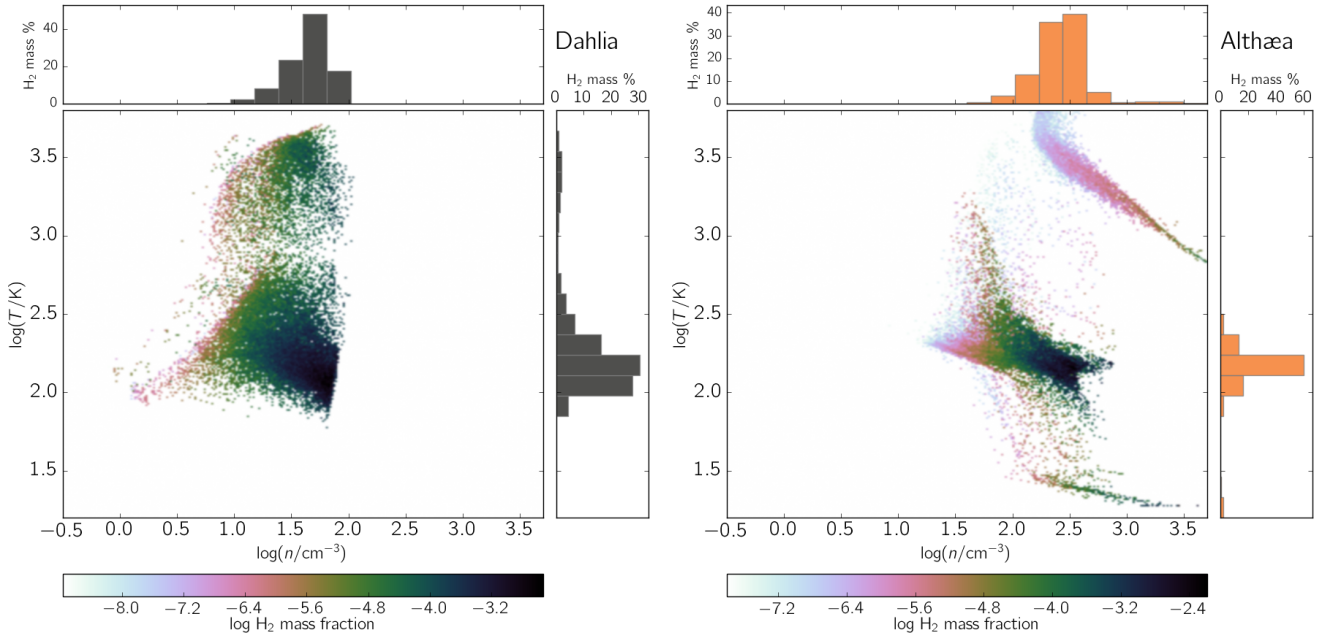


Figure 8. EOS of the molecular (H_2) gas for Dahlia (left panel) and Althæa (right panel) i.e. the H_2 mass-weighted PDF in the $n - T$ plane. Notation is similar to Fig. 7, albeit a different region of $n - T$ plane is shown.

induced by the Haardt & Madau (2012) UVB, while in Althæa is mainly due to photo-electric heating on dust grains illuminated from the uniform ISRF of intensity G . Only $\simeq 10\%$ of the gas is in a hot 10^6 K component produced by accretion shocks and SN explosions. A relatively minor

difference descends from Althæa's more effective mechanical feedback, already noted when discussing Fig. 4: small pockets of freshly produced very hot ($\geq 10^6$ K) and diffuse (0.1 cm^{-3}) gas are twice more abundant in Althæa, as it can

be appreciated from a visual inspection of the temperature maps in Fig. 5.

Fig. 7 (in particular compare the upper horizontal panels) shows that the density PDF is remarkably different in the two galaxies. In Dahlia the distribution peaks at 0.1 cm^{-3} ; Althæa instead features a bi-modal PDF with a second, similar amplitude peak at $n \simeq 100 \text{ cm}^{-3}$. This entails the fact that the dense $\gtrsim 10 \text{ cm}^{-3}$ gas is about 2 times more abundant in the latter system. In addition, the very dense gas ($n \gtrsim 300 \text{ cm}^{-3}$), only present in Althæa, can cool to temperatures of 30 K, not too far from the CMB one.

The high-density part of the PDF is worth some more insight as it describes the gas that ultimately regulates star formation. This gas is largely in molecular form, and accounts (see Tab. 1) for 1.7% (13.8%) of the total gas mass in Dahlia (Althæa). Its H_2 density-weighted distribution in the $n-T$ plane is reported in Fig. 8. On average, the H_2 gas in Dahlia is 10 times less dense than in Althæa as a result of the new non-equilibrium prescription requiring higher gas densities to reach the same f_{H_2} fraction; at the same time the warm ($T \gtrsim 10^3 \text{ K}$) H_2 fraction drops from 20% (Dahlia) to an almost negligible value. Clearly, the warm component was a spurious result as (a) H_2 cooling was not included, and (b) f_{H_2} was considered to be independent of gas temperature (see eq.s 5). Note that in Althæa traces of warm H_2 are only found at large densities, in virtually metal-free gas in which H_2 production must proceed via much less efficient gas-phase reactions rather than on dust surfaces. This tiny fraction of molecular gas can survive only if densities large enough to provide a sufficient H_2 self shielding against photodissociation are present.

Finally, the sharp EOS cutoff at $n \gtrsim 10^2 \text{ cm}^{-3}$ in Dahlia is caused by the density-threshold behavior mimicked by the enforced chemical equilibrium: above $n_c \simeq 26.45 (Z/Z_\odot)^{-0.87} \text{ cm}^{-3}$ (Sec. 2.2) the gas is rapidly turned into stars. This spurious effect disappears in Althæa, implementing a full time-dependent chemical network.

4 OBSERVATIONAL PROPERTIES

As we already mentioned, the strongest impact of different chemistry implementations is on the gas properties, and consequently on ISM-related observables. In the following, we highlight the most important among these aspects.

4.1 Schmidt-Kennicutt relation

We start by analyzing the classical Schmidt-Kennicutt (SK) relation. This comparison should be interpreted as a consistency check of the balance between SF and feedback, since in the model we assume a SFR law that mimics a SK relation (eq. 1).

The SK relation, in its most modern (Krumholz et al. 2012) formulation, links the SFR ($\dot{\Sigma}_*$) and total gas (Σ) surface density per unit free-fall time, $\dot{\Sigma}_* = \epsilon_*^{\text{ff}} \Sigma / t_{\text{ff}}$. The proportionality constant, often referred to as the efficiency per free-fall time following eq. 1, is simply $\epsilon_*^{\text{ff}} = \zeta_{\text{sf}} f_{\text{H}_2}$. Experimentally, Krumholz et al. (2012) find $\epsilon_*^{\text{ff}} = 0.015$ (see Krumholz 2015 for a complete review on the subject). This result is supported also by a larger set of observations including single MCs (Heiderman et al. 2010; Lada et al. 2010),

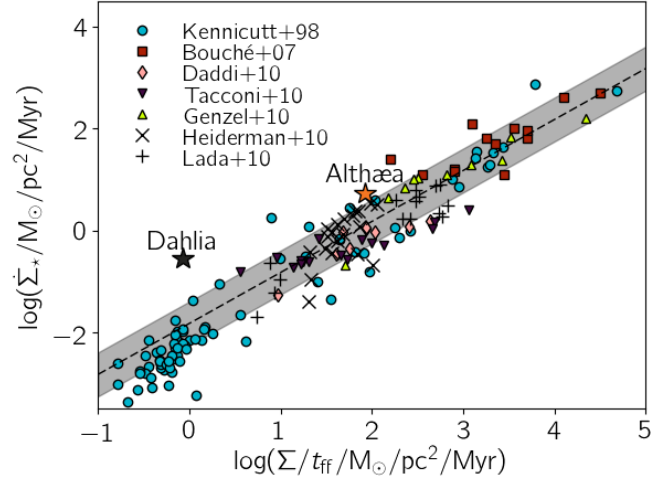


Figure 9. Comparison of the observed and simulated Schmidt-Kennicutt relation expressed in terms of $\dot{\Sigma}_* - \Sigma/t_{\text{ff}}$. Observations are taken from single MCs (Heiderman et al. 2010; Lada et al. 2010), local unresolved galaxies (Kennicutt 1998), and moderate redshift unresolved galaxies (Bouché et al. 2007; Daddi et al. 2010a,b; Tacconi et al. 2010; Genzel et al. 2010); the correlation (dispersion) for the observation found by Krumholz et al. (2012, see the text for details) is plotted with a black dashed line (grey shaded region). Dahlia and Althæa averaged value are plotted with black and orange stars, respectively (see Fig. 10 for the complete distribution in the simulated galaxies).

local unresolved galaxies (Kennicutt 1998), and moderate redshift, unresolved galaxies (Bouché et al. 2007; Daddi et al. 2010a,b; Tacconi et al. 2010; Genzel et al. 2010). The SK relation is shown in Fig. 9, along with the location of Dahlia and Althæa at $z = 6$.

Dahlia appears to be over-forming stars with respect to its gas mass, and therefore it is located about 3σ above the KS relation. As Althæa needs about 10 times higher density to sustain the same SFR, its location is closer to expectations from the SK. We have checked that the agreement is even better if we use only data relative to MC complexes (e.g. Heiderman et al. 2010; Murray 2011).

Dahlia's $\epsilon_*^{\text{ff}} = \zeta_{\text{sf}} f_{\text{H}_2}$ is similar to the analog values found by Semenov et al. (2016), who compute such efficiency using a turbulent eddy approach (Padoan et al. 2012), with no notion of molecular hydrogen fraction. The difference is that Dahlia misses the high density gas. Althæa instead matches both the ϵ_*^{ff} and the amount of high density gas found by Semenov et al. (2016). Also, its $\dot{\Sigma}_* - \Sigma$ relation is consistent with Torrey et al. (2017), who use a star formation recipe involving self-gravitating gas with a local SK H_2 dependent relation.

From our simulations it is also possible to perform a cell-by-cell analysis of the SK relation (Fig. 10). As expected, the results show the presence of a consistent spread in the local efficiency values which, however, has a different origin for Dahlia and Althæa. While in the former the variation is mostly due to a different enrichment level affecting H_2 abundance (eq. 5), for Althæa the spread is larger because it results also from the individual evolutionary histories of the cells.

As noted by Rosdahl et al. (2017), for galaxy simula-

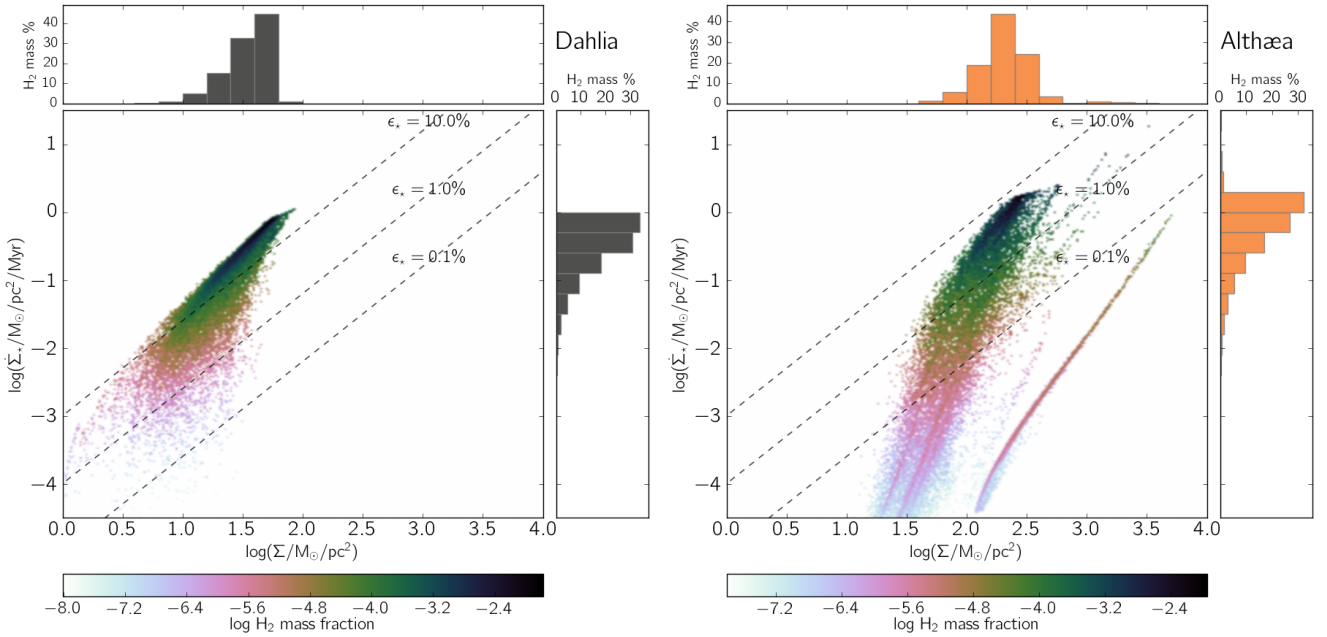


Figure 10. Schmidt-Kennicutt relation in Dahlia (left panel) and Althæa (right panel) at $t_* \simeq 700$ Myr ($z = 6$). The relation is plotted using the H_2 mass weighted PDF of the instantaneous SFR surface density ($\Sigma_*/M_\odot \text{pc}^{-2} \text{Myr}^{-1}$) versus the total gas surface density ($\Sigma/M_\odot/\text{pc}^2$). On both panels with dashed grey lines we overplot the relation observed from Kennicutt & Evans (2012), i.e. $\Sigma_* \propto \Sigma^{1.4}$, for several normalizations that written inline. Otherwise notation is similar to Figs 8 and 7.

tions with a SF model based on SK-like relation (eq. 1), the resulting $\epsilon_* = \epsilon_*^{\text{ff}}/t_{\text{ff}}$ depends on how the feedback is implemented. However, here we show that Althæa has a lower ϵ_* in spite of the fact that it implements exactly the same feedback prescription as Dahlia. The latter is qualitatively similar to a delayed cooling scheme used by Rosdahl et al. (2017) and others (Stinson et al. 2006; Teyssier et al. 2013). The lower efficiency ϵ_* is a consequence of chemistry. As under non-equilibrium conditions the gas must be denser to form H_2 , the ISM becomes more clumpy (Fig. 6). These clumps can form massive clusters of OB stars which, acting coherently, yield stronger feedback and may disrupt completely the star forming site.

4.2 Far and mid infrared emission

A meaningful way to compare the two galaxies is to predict their C II and H_2 line emission, that can be observable at high- z with ALMA, and possibly with SPICA (Spinoglio & et al. 2017; Egami & et al. 2017, in preparation), respectively. Similarly to P17, we use a modified version of the [C II] emission model from Vallini et al. (2015, hereafter V15). Such model is based on temperature, density and metallicity grids built using CLOUDY (Ferland et al. 2013), as detailed in App. B. In Fig. 11 we plot the [C II] 157.74 μm and H_2 17.03 μm surface brightness maps ($S/(L_\odot \text{kpc}^{-2})$); the field of view is the same as in Fig. 5.

4.2.1 Far infrared emission

Let us analyze first the C II emission. Dahlia has a [C II] luminosity of $\log(L_{\text{CII}}/L_\odot) \simeq 7.5$ which is about 7 times smaller than Althæa, i.e. $\log(L_{\text{CII}}/L_\odot) \simeq 8.3$.

Fig. 11 shows that the surface brightness morphology in the two galaxies is similar. Dahlia’s emission is concentrated in the disk, featuring and average surface brightness of $\log\langle S_{[\text{CII}]} / (L_\odot \text{kpc}^{-2}) \rangle \simeq 6.4$ with peaks up to $\log(S_{[\text{CII}]} / (L_\odot \text{kpc}^{-2})) \simeq 7.4$ along the spiral arms. The analogous values for Althæa are 7.3 and 8.7, respectively.

This can be explained as follows. FIR emission from the warm ($\simeq 10^4\text{K}$), low density ($\lesssim 0.1 \text{cm}^{-3}$) component of the ISM is suppressed at high- z by the CMB (Gong et al. 2012; da Cunha et al. 2013; Pallottini et al. 2015; V15; App. B), as the upper levels of the [C II] transition cannot be efficiently populated through collisions and the spin temperature of the transition approaches the CMB one (see Pallottini et al. 2015, for possibility of [C II] detection from low density gas via CMB distortions). Thus, $\simeq 95\%$ of the [C II] emission comes from dense ($\gtrsim 10 \text{cm}^{-3}$, cold ($\simeq 100\text{K}$), mostly molecular disk gas. As noted in V15 (see in particular their Fig. 4) even when the CMB effect is neglected, the diffuse gas ($\lesssim 0.1 \text{cm}^{-3}$) account only for $\lesssim 5\%$ of the emission for galaxies with SFR $\sim 100 M_\odot \text{yr}^{-1}$ and $Z \sim Z_\odot$, while it can be important in smaller objects (Olsen et al. 2015). The emissivity (in L_\odot/M_\odot) of such gas can be written as in P17 (in eq. 8, see also Vallini et al. 2013, 2017; Goicoechea et al. 2015):

$$\epsilon_{[\text{CII}]} \simeq 0.1 \left(\frac{n}{10^2 \text{cm}^{-3}} \right) \left(\frac{Z}{Z_\odot} \right). \quad (10)$$

for $n \lesssim 10^3 \text{cm}^{-3}$, i.e. the critical density for [C II] emission¹⁹. As the metallicity in the disk of the two galaxies is roughly similar ($\langle Z \rangle \simeq 0.5 Z_\odot$, see Tab. 1), difference in

¹⁹ As the suppression of the CMB affects only the diffuse component ($\lesssim 0.1 \text{cm}^{-3}$), no significant difference is expected in the

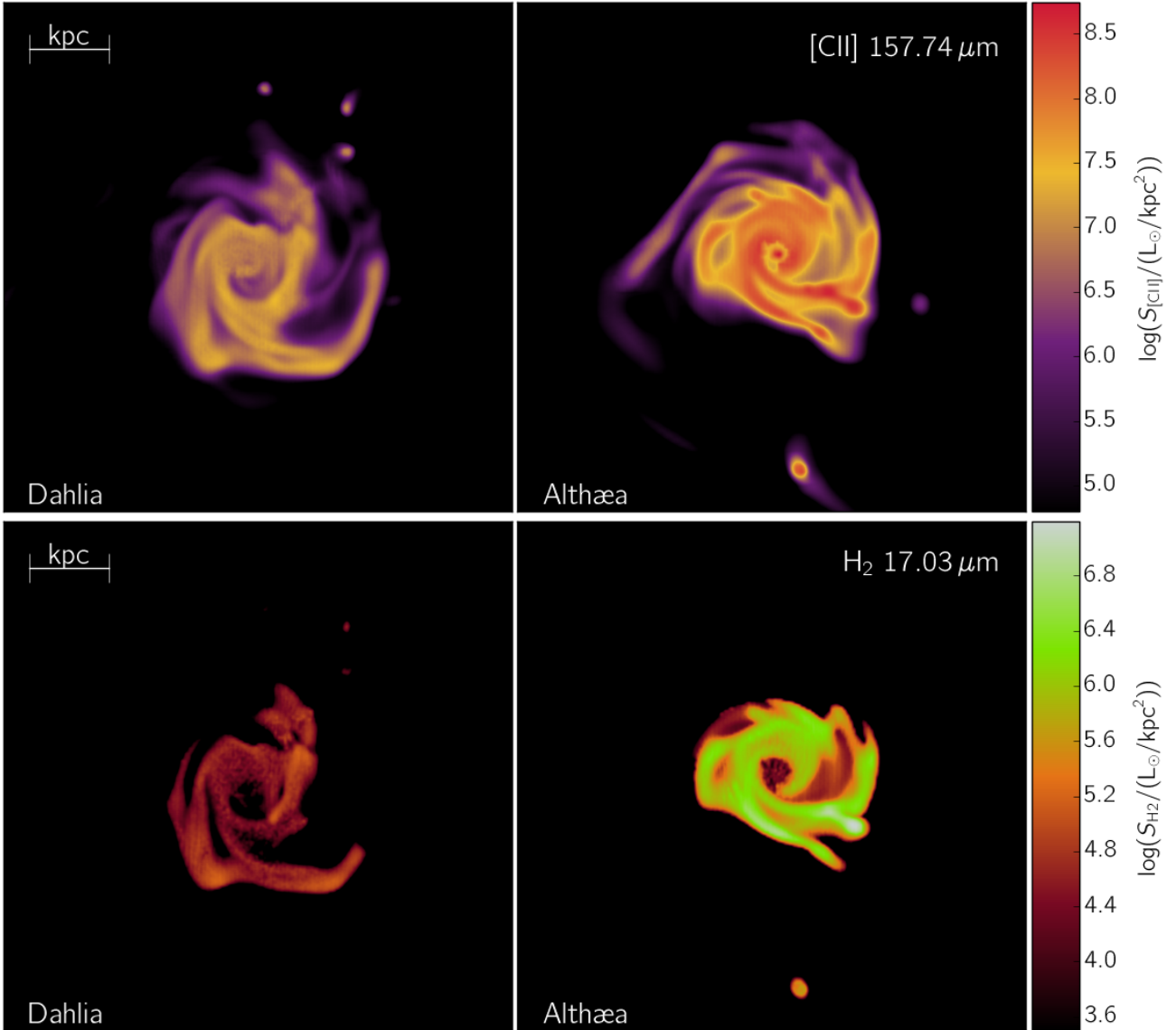


Figure 11. Synthetic emission maps¹⁶ of the simulated galaxies Dahlia (left panels) and Althæa (right panels) at age t_* \simeq 700 Myr ($z = 6$). Integrated surface brightness of [C II] ($S_{[\text{C II}]} / (L_{\odot} \text{ kpc}^{-2})$) and H₂ ($S_{\text{H}_2} / (L_{\odot} \text{ kpc}^{-2})$) are shown in the upper and lower panels, respectively. The field of view is the same as in Fig. 5.

the luminosities is entirely explained by the larger density in Althæa. We stress once again that such density variation is a result of a more precise, non-equilibrium chemical network requiring to reach much higher densities before the gas is converted to stars. It is precisely that dense gas that accounts for a larger FIR line emissivity from PDRs.

We can also compare the calculated synthetic [C II] emission vs. SFR with observations (Fig. 12) obtained for dwarf galaxies (De Looze et al. 2014), and available high- z detections or upper-limits. The [C II] emission from Dahlia is lower than expected based on the local [C II]-SFR relation; its luminosity is also well below all upper limits for high- z galaxies. Although Althæa is \simeq 10 times more luminous, even this object lies below the local relation, al-

beit only by 1.3σ . We believe that the reduced luminosity is caused by the combined effects of the CMB suppression and relatively lower Z . Note, however, that the predicted luminosity exceeds the upper limits derived for LAEs (e.g. Ouchi et al. 2013; Ota et al. 2014), but is broadly consistent with that of the handful of LBGs so far detected, like e.g. the four galaxies in the Pentericci et al. (2016). In general, observations are still rather sparse, with few [C II] detections with SFR comparable to Althæa (e.g. Capak et al. 2015). Also unclear is the amplitude of the scattering of the relation for high- z objects compared with local ones. Improvements in the understanding of the ISM structure are expected from deeper observations and/or other ions (e.g. [O III] Inoue et al. 2016; Carniani et al. 2017). Also helpful would be a larger catalogue of simulated galaxies (cfr. Ceverino et al. 2017), to control environmental effects.

emissivity from the disks of the two galaxies (eq. 10), that is composed of much higher ($\gtrsim 20 \text{ cm}^{-3}$) density material.

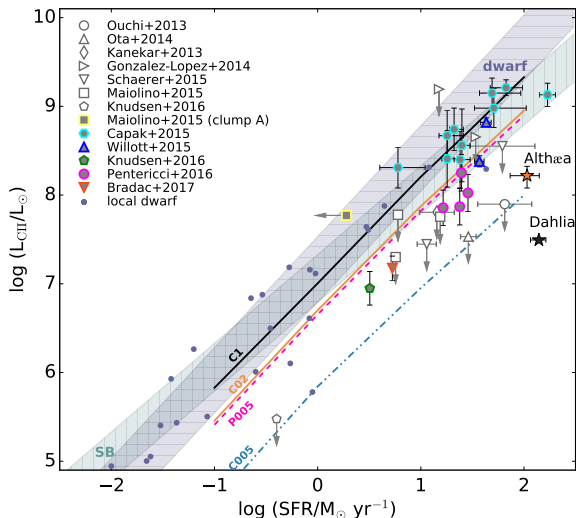


Figure 12. The [C II]-SFR relation. Shown are Althæa (orange star) and Dahlia (black) at 700 Myr or $z = 6$; the errors refers to r.m.s. variation in the last 50 Myr. Lines refer to results from the V15 model: constant metallicity models with $Z = Z_{\odot}$ (solid black), $Z = 0.2 Z_{\odot}$ (solid orange), $Z = 0.05 Z_{\odot}$ (pink dashed), and a model with mean $\langle Z/Z_{\odot} \rangle = 0.05$ + density-metallicity relation extracted from cosmological simulations (Pallottini et al. 2014b, blue dot-dashed). Data for local dwarf galaxies (De Looze et al. 2014) are plotted with little circles and the grey hatched region gives the mean and r.m.s. variation in the sample. For high- z galaxies, detections (upper-limits) are plotted with filled (empty) symbols, according to the inset legend. The high- z sample include individual galaxies as BDF-3299 (Maiolino et al. 2015; Carniani et al. 2017), HCM6A (Kanekar et al. 2013), Himiko (Ouchi et al. 2013; Ota et al. 2014), IOK-1 (Ota et al. 2014), and data from Capak et al. (2015, $z \simeq 5.5$), Willott et al. (2015, $z \simeq 6$), Schaefer et al. (2015, $z \simeq 7$), (Pentericci et al. 2016, $z \simeq 7$), González-López et al. (2014, $z \simeq 8$), and lensed $z \simeq 6.5$ galaxies from Knudsen et al. (2016) and Bradac et al. (2017).

4.2.2 Mid infrared emission

By inspecting the lower panel of Fig. 11 showing the predicted H_2 17.03 μm line emission, we come to conclusions similar to those for the [C II]. Althæa outshines Dahlia by $\simeq 15\times$ by delivering a total line luminosity of $\log(L_{H_2}/L_{\odot}) \simeq 6.5$. Differently from the [C II] case, also the deviations from the mean are much more marked in Althæa, as appreciated from the Figure.

Note that the H_2 17.03 μm line emissivity is enhanced in high density, high temperature regions. Indeed, H_2 emission mostly arises from shocked-heated molecular gas, for which $100 \lesssim n/\text{cm}^{-3} \lesssim 10^5$ and for $10 \lesssim T/\text{K} \lesssim 3000$ (see App. B).

For Dahlia, the disk density is relatively low, $n \simeq 30 \text{ cm}^{-3}$; in addition only 20% of the gas is warm enough to allow some ($\epsilon_{H_2} \simeq 0.01 L_{\odot}/M_{\odot}$) emission. In practice, such emission predominantly occurs along the outer spiral arms of the galaxy where these conditions are met due to the heating produced by SN explosions. In the denser Althæa disk, the gas emissivity can attain $\epsilon_{H_2} \simeq 10^{-3} - 0.01$ already at moderate $T = 200 \text{ K}$. The brightness peaks are associated to a few ($\lesssim 1\%$) pockets of thousand-degree gas;

they can be clearly identified in the map. This is particularly interesting because a galaxy like Althæa might be detectable at very high- z with SPICA, as suggested by Egami & et al. (2017, in preparation).

5 CONCLUSIONS

To improve our understanding of high- z galaxies we have studied the impact of H_2 chemistry on their evolution, morphology and observed properties. To this end, we compare two zoom-in galaxy simulations implementing different chemical modelling. Both simulations start from the cosmological same initial conditions, and follow the evolution of a prototypical $M_{\star} \simeq 10^{10} M_{\odot}$ galaxy at $z = 6$ resolved at the scale of giant molecular clouds (30 pc). Stars are formed according to a H_2 dependent Schmidt-Kennicutt relation. We also account for winds from massive stars, SN explosions and radiation pressure in a stellar age/metallicity dependent fashion (see Sec. 2.1). The first galaxy is named Dahlia and H_2 formation is computed from the Krumholz et al. (2009) equilibrium model; Althæa instead implements a non-equilibrium chemistry network, following Bovino et al. (2016). The key results can be summarized as follows:

- The star formation rate of the two galaxies is similar, and increases with time reaching values close to $100 M_{\odot} \text{ yr}^{-1}$ at $z = 6$ (see Fig. 2). However, Dahlia forms stars at a rate that is on average 1.5 ± 0.6 times larger than Althæa; it also shows a less prominent burst structure.
- Both galaxies at $z = 6$ have a SFR-stellar mass relation compatible with Jiang et al. (2016) observations (Fig. 3). Moreover, they both show a continuous time evolution from specific SFR of $s\text{SFR} \simeq 40 \text{ Gyr}^{-1}$ to 5 Gyr^{-1} . This is understood as an effect of the progressively increasing impact of stellar feedback hindering subsequent star formation events.
- The non-equilibrium chemical model implemented in Althæa determines the atomic to molecular hydrogen transition to occur at densities exceeding 300 cm^{-3} , i.e. about 10 times larger than predicted by equilibrium model used for Dahlia (Fig. 1). As a result, Althæa features a more clumpy and fragmented morphology (Fig. 6). This configuration makes SN feedback more effective, as noted in point (a) above (Fig. 4).
- Because of the lower density and weaker feedback, Dahlia sits 3σ away from the Schmidt-Kennicutt relation; Althæa, instead nicely agrees with observations (Fig. 9). Note that although the SF efficiency is similar in the two galaxies and consistent with other simulations (Semenov et al. 2016), Dahlia is off the relation because of insufficient molecular gas content (Fig. 8).
- We confirm that most of the emission from the C II and H_2 is due to the dense gas forming the disk of the two galaxies. Because of Dahlia's lower average density, Althæa outshines Dahlia by a factor of 7 (15) in [C II] 157.74 μm (H_2 17.03 μm) line emission (Fig. 11). Yet, Althæa has a 10 times lower [C II] luminosity than expected from the locally observed [C II]-SFR relation (Fig. 12). Whether this relation does not apply at high- z or the line luminosity is reduced by CMB and metallicity effects remains as an open questions which can be investigated with future deeper observations.

To conclude, both Dahlia and Althæa follow the ob-

served high-*z* SFR- M_* relation. However, many other observed properties (Schmidt-Kennicutt relation, C II and H₂ emission) are very different. This shows the importance of accurate, non-equilibrium implementation of chemical networks in early galaxy numerical studies.

ACKNOWLEDGMENTS

We are grateful to the participants of *The Cold Universe* program held in 2016 at the KITP, UCSB, for discussions during the workshop. We thank P. Capelo, D. Celoria, E. Egami, D. Galli, T. Grassi, L. Mayer, S. Riolo, J. Wise for interesting and stimulating discussions. We thank the authors and the community of RAMSES and PYMSES for their work. AP acknowledges support from Centro Fermi via the project CORTES, “Cosmological Radiative Transfer in Early Structures”. AF acknowledges support from the ERC Advanced Grant INTERSTELLAR H2020/740120. RM acknowledge support from the ERC Advanced Grant 695671 “QUENCH” and from the Science and Technology Facilities Council (STFC). SS acknowledges support from the European Commission through a Marie Skłodowska-Curie Fellowship, program PRIMORDIAL, Grant No. 700907. This research was supported in part by the National Science Foundation under Grant No. NSF PHY11-25915.

References

- Agertz O., Kravtsov A. V., 2015, *ApJ*, 804, 18
 Agertz O., Kravtsov A. V., Leitner S. N., Gnedin N. Y., 2013, *ApJ*, 770, 25
 Asano R. S., Takeuchi T. T., Hirashita H., Inoue A. K., 2013, *Earth, Planets, and Space*, 65, 213
 Asplund M., Grevesse N., Sauval A. J., Scott P., 2009, *ARA&A*, 47, 481
 Bakes E. L. O., Tielens A. G. G. M., 1994, *ApJ*, 427, 822
 Barai P., Monaco P., Murante G., Ragagnin A., Viel M., 2015, *MNRAS*, 447, 266
 Behroozi P. S., Wechsler R. H., Conroy C., 2013, *ApJ*, 770, 57
 Bertelli G., Bressan A., Chiosi C., Fagotto F., Nasi E., 1994, *A&A Supp.*, 106, 275
 Black J. H., 1987, in Hollenbach D. J., Thronson Jr. H. A., eds, *Astrophysics and Space Science Library Vol. 134, Interstellar Processes*. pp 731–744
 Black J. H., Dalgarno A., 1976, *ApJ*, 203, 132
 Bouché N., et al., 2007, *ApJ*, 671, 303
 Bouwens R. J., et al., 2015, *ApJ*, 803, 34
 Bovino S., Grassi T., Capelo P. R., Schleicher D. R. G., Banerjee R., 2016, *A&A*, 590, A15
 Bradac M., et al., 2017, *ApJL*, 836, L2
 Bryan G. L., et al., 2014, *ApJS*, 211, 19
 Capak P. L., et al., 2015, *Nature*, 522, 455
 Carilli C. L., Walter F., 2013, *ARA&A*, 51, 105
 Carniani S., et al., 2017, preprint, ([arXiv:1701.03468](https://arxiv.org/abs/1701.03468))
 Cazaux S., Spaans M., 2009, *A&A*, 496, 365
 Ceverino D., Klypin A., Klimek E. S., Trujillo-Gomez S., Churchill C. W., Primack J., Dekel A., 2014, *MNRAS*, 442, 1545
 Ceverino D., Glover S., Klessen R., 2017, preprint, ([arXiv:1703.02913](https://arxiv.org/abs/1703.02913))
 Choudhury T. R., Padmanabhan T., Srianand R., 2001, *MNRAS*, 322, 561
 Ciardi B., Ferrara A., 2001, *MNRAS*, 324, 648
 Coles P., Jones B., 1991, *MNRAS*, 248, 1
 Cormier D., et al., 2015, *A&A*, 578, A53
 Daddi E., et al., 2010a, *ApJ*, 713, 686
 Daddi E., et al., 2010b, *ApJL*, 714, L118
 Davé R., Finlator K., Oppenheimer B. D., 2011, *MNRAS*, 416, 1354
 De Looze I., et al., 2014, *A&A*, 568, A62
 Draine B. T., 1978, *ApJS*, 36, 595
 Dubois Y., Teyssier R., 2008, *A&A*, 477, 79
 Dunlop J. S., 2013, in Wiklind T., Mobasher B., Bromm V., eds, *Astrophysics and Space Science Library Vol. 396, Astrophysics and Space Science Library*. p. 223 ([arXiv:1205.1543](https://arxiv.org/abs/1205.1543)), doi:10.1007/978-3-642-32362-1_5
 Egami E., et al. 2017, in preparation, 0, 0
 Federrath C., Klessen R. S., 2013, *ApJ*, 763, 51
 Ferland G. J., et al., 2013, *Revista Mexicana de Astronomia y Astrofísica*, 49, 137
 Fiacconi D., Mayer L., Madau P., Lupi A., Dotti M., Haardt F., 2017, *MNRAS*, 467, 4080
 Fujimoto S., Ouchi M., Shibuya T., Nagai H., 2017, preprint, ([arXiv:1703.02138](https://arxiv.org/abs/1703.02138))
 Gallerani S., Pallottini A., Feruglio C., Ferrara A., Maiolino R., Vallini L., Riechers D. A., 2016, preprint, ([arXiv:1604.05714](https://arxiv.org/abs/1604.05714))
 Galli D., Palla F., 1998, *A&A*, 335, 403
 Gatto A., et al., 2015, *MNRAS*, 449, 1057
 Genzel R., et al., 2010, *MNRAS*, 407, 2091
 Glassgold A. E., Galli D., Padovani M., 2012, *ApJ*, 756, 157
 Gleser L., Nusser A., Ciardi B., Desjacques V., 2006, *MNRAS*, 370, 1329
 Gnedin N. Y., 2010, *ApJL*, 721, L79
 Goicoechea J. R., et al., 2015, *ApJ*, 812, 75
 Gong Y., Cooray A., Silva M., Santos M. G., Bock J., Bradford C. M., Zemcov M., 2012, *ApJ*, 745, 49
 González-López J., et al., 2014, *ApJ*, 784, 99
 González V., Labbé I., Bouwens R. J., Illingworth G., Franx M., Kriek M., Brammer G. B., 2010, *ApJ*, 713, 115
 Grassi T., Bovino S., Schleicher D. R. G., Prieto J., Seifried D., Simoncini E., Gianturco F. A., 2014, *MNRAS*, 439, 2386
 Grassi T., Bovino S., Haugbølle T., Schleicher D. R. G., 2017, *MNRAS*, 466, 1259
 Haardt F., Madau P., 2012, *ApJ*, 746, 125
 Habing H. J., 1968, *Bull. Astron. Inst. Netherlands*, 19, 421
 Hahn O., Abel T., 2011, *MNRAS*, 415, 2101
 Hartwig T., Clark P. C., Glover S. C. O., Klessen R. S., Sasaki M., 2015, *ApJ*, 799, 114
 Heiderman A., Evans II N. J., Allen L. E., Huard T., Heyer M., 2010, *ApJ*, 723, 1019
 Hirashita H., Ferrara A., 2002, *MNRAS*, 337, 921
 Hollenbach D., McKee C. F., 1979, *ApJS*, 41, 555
 Hopkins P. F., Narayanan D., Murray N., 2013, *MNRAS*, 432, 2647
 Hopkins P. F., et al., 2017, preprint, ([arXiv:1702.06148](https://arxiv.org/abs/1702.06148))
 Inoue A. K., et al., 2016, *Science*, 352, 1559
 Jiang L., et al., 2016, *ApJ*, 816, 16
 Jura M., 1975, *ApJ*, 197, 575
 Kanekar N., Wagg J., Ram Chary R., Carilli C. L., 2013, *ApJL*, 771, L20
 Katz H., Kimm T., Sijacki D., Haehnelt M., 2016, preprint, ([arXiv:1612.01786](https://arxiv.org/abs/1612.01786))
 Kennicutt Jr. R. C., 1998, *ApJ*, 498, 541
 Kennicutt R. C., Evans N. J., 2012, *ARA&A*, 50, 531
 Kim J.-h., et al., 2014, *ApJS*, 210, 14
 Kim J.-h., et al., 2016, *ApJ*, 833, 202
 Klessen R. S., Glover S. C. O., 2014, preprint, ([arXiv:1412.5182](https://arxiv.org/abs/1412.5182))
 Knudsen K. K., Richard J., Kneib J.-P., Jauzac M., Clément B., Drouart G., Egami E., Lindroos L., 2016, *MNRAS*, 462, L6
 Kroupa P., 2001, *MNRAS*, 322, 231
 Krumholz M. R., 2015, preprint, ([arXiv:1511.03457](https://arxiv.org/abs/1511.03457))

- Krumholz M. R., McKee C. F., Tumlinson J., 2008, *ApJ*, 689, 865
- Krumholz M. R., McKee C. F., Tumlinson J., 2009, *ApJ*, 693, 216
- Krumholz M. R., Dekel A., McKee C. F., 2012, *ApJ*, 745, 69
- Labadens M., Chapon D., Pomarède D., Teyssier R., 2012, in Ballester P., Egret D., Lorente N. P. F., eds, *Astronomical Society of the Pacific Conference Series Vol. 461, Astronomical Data Analysis Software and Systems XXI*. p. 837
- Lada C. J., Lombardi M., Alves J. F., 2010, *ApJ*, 724, 687
- Laporte N., et al., 2017, *ApJL*, 837, L21
- Leitherer C., et al., 1999, *ApJS*, 123, 3
- Mac Low M.-M., 1999, *ApJ*, 524, 169
- Madau P., Dickinson M., 2014, *ARA&A*, 52, 415
- Maio U., Tescari E., 2015, *MNRAS*, 453, 3798
- Maio U., Petkova M., De Lucia G., Borgani S., 2016, *MNRAS*, 460, 3733
- Maiolino R., et al., 2015, *MNRAS*, 452, 54
- Martizzi D., Faucher-Giguère C.-A., Quataert E., 2015, *MNRAS*, 450, 504
- McKee C. F., Krumholz M. R., 2010, *ApJ*, 709, 308
- Mecke K. R., Buchert T., Wagner H., 1994, *A&A*, 288, 697
- Murray N., 2011, *ApJ*, 729, 133
- Novikov D., Schmalzing J., Mukhanov V. F., 2000, *A&A*, 364, 17
- O’Shea B. W., Wise J. H., Xu H., Norman M. L., 2015, *ApJL*, 807, L12
- Olsen K. P., Greve T. R., Narayanan D., Thompson R., Toft S., Brinch C., 2015, *ApJ*, 814, 76
- Osterbrock D. E., 1989, *Astrophysics of gaseous nebulae and active galactic nuclei*. Mill Valley, CA, University Science Books
- Ostriker J. P., McKee C. F., 1988, *Reviews of Modern Physics*, 60, 1
- Ota K., et al., 2014, *ApJ*, 792, 34
- Ouchi M., et al., 2013, *ApJ*, 778, 102
- Padoan P., Haugbølle T., Nordlund Å., 2012, *ApJL*, 759, L27
- Pallottini A., Ferrara A., Gallerani S., Salvadori S., D’Odorico V., 2014a, *MNRAS*, 440, 2498
- Pallottini A., Gallerani S., Ferrara A., 2014b, *MNRAS*, 444, L105
- Pallottini A., Gallerani S., Ferrara A., Yue B., Vallini L., Maiolino R., Feruglio C., 2015, *MNRAS*, 453, 1898
- Pallottini A., Ferrara A., Gallerani S., Vallini L., Maiolino R., Salvadori S., 2017, *MNRAS*, 465, 2540
- Pentericci L., et al., 2016, *ApJL*, 829, L11
- Pérez-Montero E., 2017, *Publ. Astr. Soc. Pac.*, 129, 043001
- Petkova M., Maio U., 2012, *MNRAS*, 422, 3067
- Planck Collaboration et al., 2014, *A&A*, 571, A16
- Rahmati A., Pawlik A. H., Raicevic M., Schaye J., 2013, *MNRAS*, 430, 2427
- Rasera Y., Teyssier R., 2006, *A&A*, 445, 1
- Rey-Raposo R., Dobbs C., Agertz O., Alig C., 2017, *MNRAS*, 464, 3536
- Richings A. J., Schaye J., Oppenheimer B. D., 2014, *MNRAS*, 442, 2780
- Rosdahl J., Schaye J., Teyssier R., Agertz O., 2015, *MNRAS*, 451, 34
- Rosdahl J., Schaye J., Dubois Y., Kimm T., Teyssier R., 2017, *MNRAS*, 466, 11
- Roskar R., Teyssier R., Agertz O., Wetzstein M., Moore B., 2014, *MNRAS*, 444, 2837
- Roussel H., et al., 2007, *ApJ*, 669, 959
- Scannapieco C., et al., 2012, *MNRAS*, 423, 1726
- Schaerer D., Boone F., Zamojski M., Staguhn J., Dessauges-Zavadsky M., Finkelstein S., Combes F., 2015, *A&A*, 574, A19
- Schmalzing J., Buchert T., 1997, *ApJL*, 482, L1
- Schmalzing J., Gorski K. M., 1998, *MNRAS*, 297, 355
- Schmidt M., 1959, *ApJ*, 129, 243
- Semenov V. A., Kravtsov A. V., Gnedin N. Y., 2016, *ApJ*, 826, 200
- Shibuya T., Ouchi M., Harikane Y., 2015, *ApJS*, 219, 15
- Smith B. D., et al., 2017, *MNRAS*, 466, 2217
- Spinoglio L., et al. 2017, in preparation, 0, 0
- Stanway E. R., 2017, preprint, ([arXiv:1702.07303](https://arxiv.org/abs/1702.07303))
- Stasińska G., 2007, preprint, ([arXiv:0704.0348](https://arxiv.org/abs/0704.0348))
- Stinson G., Seth A., Katz N., Wadsley J., Governato F., Quinn T., 2006, *MNRAS*, 373, 1074
- Tacconi L. J., et al., 2010, *Nature*, 463, 781
- Teyssier R., 2002, *A&A*, 385, 337
- Teyssier R., Pontzen A., Dubois Y., Read J. I., 2013, *MNRAS*, 429, 3068
- Timmermann R., Bertoldi F., Wright C. M., Drapatz S., Draine B. T., Haser L., Sternberg A., 1996, *A&A*, 315, L281
- Tomassetti M., Porciani C., Romano-Díaz E., Ludlow A. D., 2015, *MNRAS*, 446, 3330
- Torrey P., Hopkins P. F., Faucher-Giguère C.-A., Vogelsberger M., Quataert E., Keres D., Murray N., 2017, *MNRAS*, 467, 2301
- Turner J., Kirby-Docken K., Dalgarno A., 1977, *ApJS*, 35, 281
- Valle G., Ferrini F., Galli D., Shore S. N., 2002, *ApJ*, 566, 252
- Vallini L., Gallerani S., Ferrara A., Baek S., 2013, *MNRAS*, 433, 1567
- Vallini L., Gallerani S., Ferrara A., Pallottini A., Yue B., 2015, *ApJ*, 813, 36
- Vallini L., Ferrara A., Pallottini A., Gallerani S., 2017, *MNRAS*, Verner D. A., Ferland G. J., 1996, *ApJS*, 103, 467
- Wakelam V., et al., 2012, *ApJS*, 199, 21
- Watson D., Christensen L., Knudsen K. K., Richard J., Gallazzi A., Michałowski M. J., 2015, *Nature*, 519, 327
- Weaver R., McCray R., Castor J., Shapiro P., Moore R., 1977, *ApJ*, 218, 377
- Webber W. R., 1998, *ApJ*, 506, 329
- Weingartner J. C., Draine B. T., 2001, *ApJ*, 563, 842
- Willott C. J., Carilli C. L., Wagg J., Wang R., 2015, *ApJ*, 807, 180
- Wise J. H., Abel T., Turk M. J., Norman M. L., Smith B. D., 2012, *MNRAS*, 427, 311
- Wolcott-Green J., Haiman Z., Bryan G. L., 2011, *MNRAS*, 418, 838
- Wolfire M. G., McKee C. F., Hollenbach D., Tielens A. G. G. M., 2003, *ApJ*, 587, 278
- Yoshiura S., Shimabukuro H., Takahashi K., Matsubara T., 2017, *MNRAS*, 465, 394
- da Cunha E., et al., 2013, *ApJ*, 766, 13

This paper has been typeset from a $\text{\TeX}/\text{\LaTeX}$ file prepared by the author.

APPENDIX A: MINKOWSKY FUNCTIONALS

In general, Minkowsky functionals are mathematical tools that give a complete characterization of the morphology of a $\mathbb{R}^n \mapsto \mathbb{R}$ field. In astrophysics they have been proposed as a mean to give a description of the large scale structure (e.g. Mecke et al. 1994), to study the topology of H II bubbles for reionization studies (e.g. Gleser et al. 2006; Yoshiura et al. 2017), and (for $n = 2$ fields) analyze CMB anisotropies and non-gaussianity (e.g. Schmalzing & Gorski 1998; Novikov et al. 2000).

A formal definition can be given following Schmalzing & Buchert (1997). Let $u(\mathbf{x})$ denote a scalar field defined on a subset of \mathbb{R}^3 with volume V . Let us take u such that it has zero mean ($\langle u(\mathbf{x}) \rangle = 0$) and variance $\langle u^2(\mathbf{x}) \rangle = \sigma$. Then we can define the excursion set $F_\nu(\mathbf{x})$ as the ensemble of regions in V satisfying $u(\mathbf{x}) > \nu\sigma$. Then, the Minkowsky functionals can be defined in

terms of volume (d^3x) and surface (d^2x) integrals as a function of the threshold ν :

$$V_0(\nu) = (V)^{-1} \int_V \Theta(u - \nu\sigma) d^3x \quad (\text{A1a})$$

$$V_1(\nu) = (6V)^{-1} \int_{\partial F_\nu} d^2x \quad (\text{A1b})$$

$$V_2(\nu) = (6\pi V)^{-1} \int_{\partial F_\nu} (\kappa_1 + \kappa_2) d^2x \quad (\text{A1c})$$

$$V_3(\nu) = (4\pi V)^{-1} \int_{\partial F_\nu} \kappa_1 \kappa_2 d^2x, \quad (\text{A1d})$$

where Θ is the Heaviside function, $\partial F_\nu(\mathbf{x})$ the surface bounding the excursion set F_ν , and $\kappa_1(\mathbf{x})$ and $\kappa_2(\mathbf{x})$ the two principal curvatures of the surface. In practical terms, V_0 is a measure of the volume filling factor of the excursion set with threshold ν , V_1 of the surface, V_2 of the mean curvature (sphericity/concavity) and V_3 of the Euler characteristic (shape of components).

The curvatures on the surface ∂F_ν can be expressed via the Koenderink invariant (Gleser et al. 2006, see appendix A and reference therein): by adopting the Einstein sum convention we can write

$$\kappa_1 + \kappa_2 = \epsilon^{ijk} \epsilon^{lmn} \delta_{kn} (\partial_i u) (\partial_j \partial_l u) (\partial_m u) / N_t^3 \quad (\text{A2a})$$

$$2\kappa_1 \kappa_2 = \epsilon^{ijk} \epsilon^{lmn} (\partial_i u) (\partial_l u) (\partial_j \partial_m u) (\partial_k \partial_n u) / N_t^2 \quad (\text{A2b})$$

$$N_t = (\partial_p u) (\partial^p u), \quad (\text{A2c})$$

where ϵ_{ijk} is the Levi-Civita symbol, δ_{ij} is the Kronecker delta, and ∂_i is the i -th component of the partial derivative operator. Finally, eq.s A1 can be suitably expressed as integral over the volume by using the following relation

$$\int_{\partial F_\nu} d^2x = \int_V \delta(u - \nu\sigma) N_t^{1/2} d^3x, \quad (\text{A3})$$

where δ is the Dirac delta.

As an illustrative example, we can compute the Minkowsky functionals for a zero-mean Gaussian random field $u \equiv \log \Delta$ with variance $\sigma^2 = \langle \log \Delta^2 \rangle$ and variance of the tangent field $\sigma_t^2 = \langle (\partial_p \log \Delta) (\partial^p \log \Delta) \rangle$. For such Gaussian field, the Minkowsky functionals can be expressed using the following analytical expression (Schmalzing & Buchert 1997, see also Gleser et al. 2006)

$$V_0 = 1/2 - c_0 \int_0^\nu \exp(-x^2/2) dx \quad (\text{A4a})$$

$$V_1 = c_1 \lambda \exp(-\nu^2/2) \quad (\text{A4b})$$

$$V_2 = c_2 \lambda^2 \nu \exp(-\nu^2/2) \quad (\text{A4c})$$

$$V_3 = c_3 \lambda^3 (\nu^2 - 1) \exp(-\nu^2/2), \quad (\text{A4d})$$

where $\nu = \log \Delta / \sigma$, $\lambda = (6\pi)^{-1/2} \sigma_t / \sigma$, and c_i are numerical constant with values $c_0 = c_3 = (2\pi)^{-1/2}$ and $c_1 = c_2 = 2/(3(2\pi)^{1/2})$.

We numerically compute the Minkowsky functionals for the $\log \Delta$ field with $\sigma = 1$ on a 256^3 unigrid box with volume $(10 \text{ Mpc})^3$, that thus result in a tangent field variance of $\sigma_t \simeq 5.6/\text{kpc}$. The resulting Minkowsky functionals are plotted in Fig. A1. We find a very good match with the analytical values.

Since the chosen $\log \Delta$ Gaussian field is an approximation to the quasi-linear regime of the cosmic density field (e.g. Coles & Jones 1991; Choudhury et al. 2001), it is intuitive to analyze the properties of its Minkowsky functionals. In Fig. A1 the filling factor V_0 gives the probability of finding regions with increasing overdensity Δ ; note that at $\Delta = 1$ (mean density), $V_0 = 0.5$, i.e. it is equiprobable to find voids ($\log \Delta \lesssim -1$) and overdense regions ($\log \Delta \gtrsim 1$). Both voids and overdense regions are isolated $V_3(\gtrsim 1) = V_3(\lesssim -1) > 0$ and have a smaller area with respect to mean density regions ($V_1(\gtrsim 1) = V_1(\lesssim -1) \lesssim V_1(0)$). However, while overdensities have spherical shapes $V_2(\gtrsim 1) > 0$, voids are concave regions ($V_2(\gtrsim 1) < 0$): both voids and overdense regions are delimited by connected ($V_2(\simeq 0) < 0$) mean density regions,

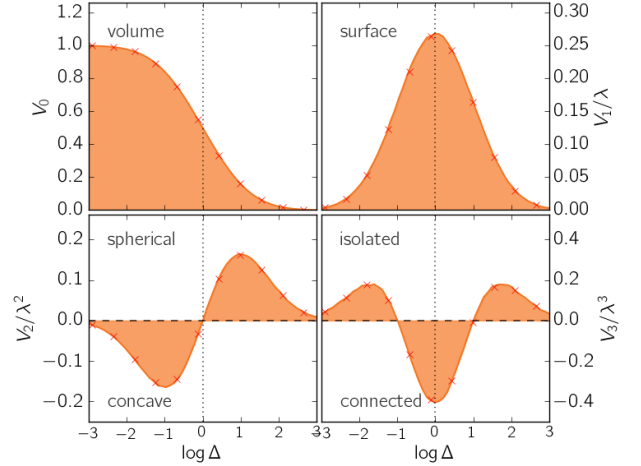


Figure A1. Example of Minkowsky functionals calculated for the zero-mean Gaussian random field $\log \Delta$. The functionals are plotted with a orange line and transparent region and are normalized by V_i/λ^i , with $\lambda = (6\pi)^{-1/2} \sigma_t / \sigma$, where $\sigma = 1$ is the field variance and $\sigma_t \simeq 5.6/\text{kpc}$ is the variance of the tangent field. Analytical expected values for the functionals (eq.s A4a) are plotted with red crosses. To guide the eye, $\log \Delta = 0$ is marked with a dotted vertical black line, and both $V_2 = 0$ and $V_3 = 0$ are highlighted with dashed horizontal lines.

that are almost flat ($V_2(\simeq 0) \simeq 0$) and have very large surface areas.

APPENDIX B: EMISSION FROM C II AND H₂.

To compute the emission from C II ions and H₂ molecules, we post-process the simulation outputs using the photoionization code CLOUDY (Ferland et al. 2013), similarly to what done in V15 and P17. We consider a grid of models based on the density (n), temperature (T) and metallicity (Z) of the gas in our simulation. We produce a total of 10^3 models, that are parameterized as a function of the column density (N). For each model we adopt a plane-parallel geometry and assume a dust content proportional to the metallicity.

The radiation field includes the CMB background and an interstellar radiation field produced by stars, that is obtained by rescaling the Milky Way spectrum (Black 1987) using the main galaxy (Dahlia or Althæa) SFR. At $z = 6$ Dahlia has a star formation rate SFR = $156 M_\odot \text{ yr}^{-1}$ and Althæa has SFR = $136 M_\odot \text{ yr}^{-1}$, where the uncertainty is the r.m.s. in the last 50 Myr (Sec. 3.1, in particular see Fig. 2). For modelling convenience, in the CLOUDY calculation we set SFR = $100 M_\odot \text{ yr}^{-1}$. Note that a larger value for the rescaling does not yield a large variation of the expected [C II] in molecular gas (Vallini et al. 2017, with $G = G_0 \text{ SFR} / M_\odot \text{ yr}^{-1}$), and H₂ emission is relatively unaffected by the field, as the excitation is mostly due to shocks (e.g. Black & Dalgarno 1976; Ciardi & Ferrara 2001).

As noted in Sec. 2.3, accounting for the UVB is not relevant for the ionization state of the gas in the proximity of galaxies (Gnedin 2010). Thus, in our CLOUDY models we consider that the gas is shielded by a column density of $N \simeq 10^{20} \text{ cm}^{-2}$.

Regarding the [C II] we underline that the effect of CMB suppression of [C II] is included in the V15 model (da Cunha et al. 2013; Pallottini et al. 2015, see also). Such effect suppress the emission where the spin temperature of the [C II] transition is close to the CMB one. This is relevant for low density ($n \lesssim 10^{-1} \text{ cm}^{-3}$) medium, that does not have enough collisions

to decouple from the CMB. Here we do not account for the photo-evaporation effect on MC, that has an important impact on FIR emission (Vallini et al. 2017), particularly when including a spatially varying FUV field, not included in the present modelling.

Even though in the present paper we only show the H₂ line at $\lambda = 17.04 \mu\text{m}$ (Sec. 4, in particular see Fig. 11), we used CLOUDY to compute the emission of the following H₂ roto-vibrational lines: 0-0 S(0), 0-0 S(1), 0-0 S(5), and 1-0 S(1), that correspond to transition of wavelength $\lambda/\mu\text{m} = 2.12, 6.91, 9.66, 17.04,$ and $28.22,$ respectively (see Spinoglio & et al. 2017; Egami & et al. 2017, in preparation).

For the considered five transitions, the oscillator strength is a decreasing function of λ (e.g. Turner et al. 1977), going from $\simeq 3 \times 10^{-7} \text{s}^{-1}$ for $\lambda = 2.12 \mu\text{m}$ to $\simeq 3 \times 10^{-11} \text{s}^{-1}$ for $\lambda = 28.22 \mu\text{m}$. On the other hand, both the excitation temperature (Timmermann et al. 1996) and the critical density for collisional excitation (Roussel et al. 2007) decrease for decreasing λ (see also Black & Dalgarno 1976), e.g. for $\lambda = 2.12 \mu\text{m}$ we have an excitation temperature $T_{\text{ex}} \simeq 6 \times 10^4 \text{K}$ and a critical density $n_{\text{cr}} \simeq 10^4 \text{cm}^{-3}$, while for $\lambda = 28.22 \mu\text{m}$ we have $T_{\text{ex}} \simeq 5 \times 10^3 \text{K}$ and $n_{\text{cr}} \simeq 5 \text{cm}^{-3}$. In the simulations the bulk of the H₂ gas have $\langle T \rangle \sim 10^2 \text{K}$ and density in the range $10^2 \lesssim n/\text{cm}^{-3} \lesssim 10^3$ (see Fig. 8); thus in both Dahlia and Althæa the most favoured H₂ transition is the $\lambda = 17.03 \mu\text{m}$, followed by the $28.21 \mu\text{m}$ line.